1   **Revision 1**

2

3   # Coupled hydrogen and fluorine incorporation in garnet: new

4   # constraints from FTIR, ERDA, SIMS, and EPMA

5

6

7   JED L. MOSENFELDER[1]*, ANETTE VON DER HANDT[1], ANTHONY C. WITHERS[2],

8   HÉLÈNE BUREAU[3], CAROLINE RAEPSAET[4], and GEORGE R. ROSSMAN[5]

9
10

11

12   [1] Department of Earth and Environmental Sciences, University of Minnesota, 116 Church St. SE,

13   Minneapolis, Minnesota, 55455, U.S.A.

14   [2] Bayerisches Geoinstitut, Universität Bayreuth, 95440 Bayreuth, Germany.

15   [3] Institut de Minéralogie, de Physique des Matériaux et de Cosmochimie (IMPMC), Sorbonne

16   Université, CNRS UMR 7590, Muséum National d'Histoire Naturelle, 4 place Jussieu, 75252

17   Paris Cedex 05, France.

18   [4] Service de Physique de l'état Condensé, SPEC, CEA, CNRS, Université Paris-Saclay, CEA

19   Saclay, 91191 Gif sur Yvette, CEDEX, France.

20   [5] Division of Geological and Planetary Sciences, California Institute of Technology, M/C 170-25,

21   Pasadena, California 91125-2500, U.S.A.

22

23   Word count: 13,992 (including abstract, references, and figure captions)

24   * E-mail: jmosenfe@umn.edu

25

26

27

ABSTRACT

29   It is well known that some garnet compositions can incorporate hydrogen and/or fluorine

30   at levels up to several weight percent. However, accurate measurement of these elements can be

31   difficult at trace to minor levels of abundance so they are frequently ignored in routine chemical

32   analysis. Furthermore, the mechanisms of H incorporation are still under debate and only one

33   mechanism for F substitution is commonly considered. We employed infrared spectroscopy

34   (FTIR), elastic recoil detection analysis (ERDA), secondary ion mass spectrometry (SIMS), and

35   electron probe microanalysis (EPMA) to measure H and F concentrations and constrain

36   incorporation mechanisms in ten grossular garnets. We also present SIMS data for 11 spessartine

37   and two andradite garnets. Three grossular garnets were measured with ERDA to obtain an

38   infrared integral molar absorption coefficient (ε_i) for H_2O of 13,470 L $\cdot$ mol^{-1} $\cdot$ cm^{-2}. Grossular

39   H_2O and F concentrations range from 0.017 to 0.133 wt% and 0.012 to 0.248 wt%, respectively.

40   Correlations between ^{16}OH and ^{19}F and interpretation of FTIR spectra prompt us to consider

41   various coupled substitutions of H and F for Si, which can explain some high frequency IR

42   absorption bands that have been attributed previously to "hydrogrossular clusters" (variably-

43   sized clusters in which 4H substitute for Si) or to inclusions of hydrous minerals. A strong

44   correlation between ^{16}OH and ^{19}F in spessartine and similar high-frequency IR bands implies a

45   similar role for H-F substitution. Coupled H-F substitution is also probably relevant to some

46   andradite-rich garnets, rare pyrope from the Dora Maira massif, and some synthetic garnets.

47   Improvements in analytical methods for trace to minor H and F open up more possibilities for

48   using these elements to calculate the activities of H_2O and F-species in fluids that were in

2

Always consult and cite the final, published document. See http:/www.minsocam.org or GeoscienceWorld

49 equilibrium with garnet-bearing phase assemblages, as well as constraining the recycling of these

50 elements into the mantle via study of xenoliths.

51

52   **INTRODUCTION**

53   Considerable progress has been made in the last three decades in understanding how trace

54 amounts of hydrogen can be incorporated in nominally anhydrous minerals, and how this H

55 (most commonly incorporated as structurally bound OH^- groups) affects geophysical and

56 petrologic processes in the Earth and other planetary bodies. Recent work has also highlighted

57 the potential importance of trace fluorine (substituting for O^{2-}) in nominally anhydrous minerals

58 (Hervig and Bell 2005; Mosenfelder et al. 2011, 2015; Beyer et al. 2012; Bernini et al. 2012;

59 Dalou et al. 2012; Mosenfelder and Rossman 2013a,b; Crépisson et al. 2014; Roberge et al.

60 2015; Grützner et al. 2017; Klemme and Stalder 2018; Yoshino and Vazhakuttiyakam 2018). In

61 the case of garnets, a diverse supergroup of minerals widely distributed in the crust and mantle of

62 the Earth, it has long been recognized that both H and F can be structurally incorporated at levels

63 up to several weight percent (see Grew et al. 2013 for review). Researchers have taken advantage

64 of this phenomenon to constrain the activities of H_2O and F-species in fluids in equilibrium with

65 garnet-bearing phase assemblages (Manning and Bird 1990; Visser 1993; Arredondo et al. 2001;

66 Chakhmouradian et al. 2008).

67   Hydrogen and/or F may in fact be almost ubiquitously present in trace to minor amounts

68 in garnets, but are commonly ignored during chemical analysis because of difficulties inherent in

69 measuring trace concentrations of light elements with commonly available techniques such as

70 electron probe microanalysis (EPMA). Note that when we specify "H_2O" or "H" concentrations

71 in this paper we are primarily referring to the equivalent in structurally bound OH^- groups,

72 because H is not incorporated in the form of structurally-bound H_2O groups in garnet.

73   Hydrogen can be detected easily using Fourier transform infrared spectroscopy (FTIR) in

74 transmission mode, which also provides information on incorporation mechanisms, but

75 uncertainties remain in absolute quantification using this method (Maldener et al. 2003; Rossman

76 2006). One of the best microanalytical techniques for trace F is secondary ion mass spectrometry

77 (SIMS), which is highly sensitive owing to the ionization efficiency of both $^{19}F^-$ and $^{19}F^+$ and has

78 benefited from technical advances that lower detection limits to less than 1 µg/g (Hauri et al.

79 2002; Koga et al. 2003; Mosenfelder et al. 2011). However, these measurements are most

80 commonly made using F-bearing glasses for calibration, which can result in working curves with

81 large uncertainties (Mosenfelder and Rossman 2013a).

82   SIMS measurements of H in garnets have primarily concentrated on pyrope-rich

83 compositions representative of the mantle (Koga et al. 2003; Aubaud et al. 2007; Tenner et al.

84 2009), with one more recent study on grossular and spessartine (Reynes et al. 2018). Quantitative

85 SIMS analyses of F in garnets are even more sparse (Jamtveit and Hervig 1994; Schingaro et al.

86 2016). In this study, we present new SIMS, FTIR, and EPMA data on the H and F concentrations

87 of ten natural grossular garnets, and SIMS data on 11 spessartine and two andradite crystals.

88 Furthermore, based on elastic recoil detection analysis (ERDA) of three grossular samples, we

89 reassess calibrations for the IR molar absorption coefficient for H_2O derived by Rossman and

90 Aines (1991) and Maldener et al. (2003). We demonstrate that H and F concentrations are

91 strongly correlated in some garnets and suggest coupled H-F incorporation mechanisms

92 analogous to those proposed for olivine by Crépisson et al. (2014). Coupled H-F substitution can

93 rectify unexplained aspects of previous incorporation models for H in grossular, spessartine, and

94   pyrope (Aines and Rossman 1984; Rossman and Aines 1991; Cho and Rossman 1993; Reynes et

95   al. 2018; Geiger and Rossman 2018, 2020a, 2020b).

96

97   **ANALYTICAL METHODS**

98   **Sample selection and preparation**

99   Table 1 lists the localities of the grossular garnets chosen for this study. Six of these

100   garnets, derived from granulites of the Neoproterozoic Mozambqiue belt in Tanzania and Kenya

101   (Giuliani et al. 2008, 2011), are referred to as "East African" in this paper. Additional details on

102   the grossular, spessartine, and andradite samples used in the study are provided in the

103   supplementary material.

104   Samples were prepared for analysis using previously described, epoxy-free polishing

105   methods and cleaning procedures (Mosenfelder et al. 2011). The garnets were fabricated into

106   doubly polished slabs that were first measured by FTIR and then sliced using a wire saw into

107   multiple chips for analysis by different techniques; in all cases, individual chips originated from

108   the same single crystal.

109

110   **FTIR**

111   Unpolarized infrared absorption spectra were collected for most of the garnets using the

112   main compartment of either a Nicolet Magna 860 FTIR or Thermo-Nicolet iS50 FTIR at Caltech.

113   All measurements employed a GLOBAR IR source, a KBr beamsplitter, and a MCT-A detector,

114   with at least 512 scans taken at 2 cm^{-1} resolution. Analysis areas were selected using 200 to 400

115   μm diameter circular apertures and multiple spectra for each crystal were taken to assess the

116   possibility of zoning. Sample thicknesses were measured using a Mitutoyo digital micrometer,

117 with a precision of ±2 μm. JLM83a was measured at UMN using a Hyperion 2000 microscope

118 attached to a Bruker Tensor 37 spectrometer, with a GLOBAR IR source, a KBr beamsplitter,

119 and a MCT-A detector. These spectra were collected on a slab ~390 μm thick, with 64 scans at 2

120 cm^{-1} resolution, using a 100 $μm^2$ square knife-edge aperture. The video-assisted mapping feature

121 of the OPUS 7.2 software was employed to take regularly spaced data (in a 6 x 8 grid) across the

122 central portion of the sample slab.

123 The low temperature (77 K) spectrum of GRR1386 was obtained in 1994 using a

124 homebuilt vacuum chamber in the main compartment of the Nicolet 60SX FTIR that was

125 operational at that time at Caltech. The room temperature spectrum of the sample taken in 1994

126 closely matches more recently acquired spectra.

127 Details of our baseline correction methods are provided in the supplementary material.

128 After baseline correction, we calculated total integrated band areas in the O-H stretching region,

129 referred to hereafter as Abs_{tot} (considered here as absorbance/cm^2 in one direction, rather than

130 multiplying one measurement by three as in some studies on garnets). Spectra were then curve

131 fitted using the Multipeak Fitting 2 package in Igor Pro software. Table 1 also gives values for

132 the weighted mean wavenumber (as defined by Libowitzky and Rossman 1997) for each

133 spectrum.

134

135 **ERDA**

136 In Table 2 we report hydrogen concentrations measured by ERDA for three grossular

137 samples (GRR732, GRR771, and GRR1756), one synthetic forsterite (GRR1017), and three

138 synthetic, rhyolitic glasses (NSL1, N3, and N5). The analyses were conducted at the Laboratoire

139 d'Etudes des Eléments Légers, CEA, Saclay, France using improved methods for micro-ERDA

140   (Raepsaet et al. 2008, Bureau et al. 2009). Analytical methods followed those outlined by

141   Withers et al. (2012) and are detailed in the supplementary material. GRR1017, well-

142   characterized as an ultra-dry reference material with ≤0.007 µg/g H_2O (Mosenfelder et al. 2011),

143   was used to assess the H background. Water contents of the rhyolitic glasses were previously

144   reported in Tenner et al. (2009), measured using Karl-Fischer titration as described in Withers

145   and Behrens (1999).

146

147   **SIMS**

148   SIMS data (Table 3) were obtained on the CAMECA 7f-GEO at Caltech using a Cs^+

149   primary ion beam and previously described methods optimized for collecting low-blank H and F

150   analyses (Mosenfelder and Rossman 2013a; Mosenfelder et al. 2011, 2015). Data are presented

151   from two sessions, conducted in 2012 and 2016. For each analysis, we acquired either 30 cycles

152   (in 2012) or 20 cycles (in 2016) through the mass sequence ^{12}C, $^{16}O^1H$, ^{18}O, ^{19}F, and ^{30}Si,

153   collecting negative ions with a mass resolution of ~5500 (∆M/M), sufficient to separate $^{16}O^1H$

154   from ^{17}O and $^{18}O^1H$ from ^{19}F (Burdo and Morrison 1971). Analyses from 2012 were obtained

155   from garnets pressed into the same indium mount as the orthopyroxenes, clinopyroxenes,

156   olivines, and F-bearing glasses (MPI-DING glasses KL2-G and ML3B-G and USGS glasses

157   BCR-2G and BHVO-2G) reported on previously (and analyzed during the same session) by

158   Mosenfelder and Rossman (2013a,b). Some of the garnets were then extracted, re-polished,

159   cleaned, and pressed together into a new indium mount with one additional garnet (JLM83a), the

160   MPI-DING and USGS glasses, and five additional F-bearing glasses (Fba-1, 2, 3, 4 and 5)

161   prepared by Guggino et al. (2011). We used the Fba-series glasses to reevaluate the F

162   concentrations of our MPI-DING and USGS glass splits, as described in Mosenfelder et al.

7

163   (2020). The revised reference values used to establish working curves for F are given in the

164   supplementary material.

165         $^{16}O^1H/^{18}O$ and $^{19}F/^{18}O$ ratios in Table 3 were blank corrected using $^{16}O^1H$ and ^{19}F

166   backgrounds monitored by analyzing "blank" reference materials: synthetic forsterite GRR1017

167   (Mosenfelder et al. 2011), a natural Cr-rich pyrope from Ugelvik, Norway (GRR332), and

168   laboratory-dehydrated grossular (GRR1122-HT) and spessartine (GRR2215-HT). Details on

169   characterization of these samples are provided in the supplementary material.

170

171   **EPMA**

172   Electron microprobe analyses (Table 4) for most samples were acquired using a JEOL

173   JXA-8900R at UMN. We first measured F, using MgF_2 as a standard; other elements were

174   subsequently analyzed on the same spots using different analytical conditions. F kα was acquired

175   on three TAP crystals simultaneously and intensities were then aggregated and combined with

176   the other elements during post-processing with Probe for EPMA software (Probesoftware, Inc.).

177   Despite its lower sensitivity for F Kα, we prefer TAP over LDE1 for this application, because

178   LDE1 has the inherent problem of significant background interferences between the F Kα and Fe

179   Kα, Mg Kβ, and Mn Kα X-ray lines (e.g., Witter and Kuehner 2004; Zhang et al. 2016). We

180   found that an accelerating voltage of 20 kV optimized fluorescence yields and peak-to-

181   background ratios for F on TAP. For most of the garnets, a beam current of 250 nA and beam

182   diameter of 10 μm was used for this stage of the analysis. Analyses of JLM83a were conducted

183   at either 200, 250, or 400 nA. Calculated detection limits range from ~40 at the highest current to

184   60 μg/g at the lowest current.

185   Using the procedure outlined by Donovan et al. (2011), an exponential background was

186   fit to the F kα peak with parameters based on a detailed wavescan of Asbestos grossular.

187   Counting times for each spectrometer were 400 seconds on peak and 350 seconds on each

188   background position, resulting in aggregated times per analysis of 1200 seconds on peak and

189   2100 seconds on the background measurement. Time-dependent intensity (TDI) loss (or gain)

190   was monitored for all elements, but no significant or systematic dependence was found so the

191   TDI correction was not used. Unknown and standard intensities were corrected for deadtime and

192   standard intensities were corrected for standard drift over time.

193   Major and minor elements were measured using an accelerating voltage of 15 kV, a beam

194   current of 20 nA, and a beam diameter of 1 μm. Counting times for each element were 20

195   seconds on peak and 10 seconds at each background position. Reference materials used for

196   calibration included synthetic forsterite (GRR1017) and tephroite (GRR392) for Mg and Mn,

197   respectively; a natural almandine (Harvard 112140) for Fe; Asbestos grossular for Ca and Si;

198   chromite (NMNH 117075) for Cr; ilmenite (NMNH 96189) for Ti; Brazilian spessartine (Verma,

199   1960) for Al; and vanadium metal for V. Na and K were also analyzed but were below the

200   detection limit in all samples.

201   Final data processing used the CITZAF matrix correction method (Armstrong 1988), with

202   FFAST mass absorption coefficients (Chantler et al. 2005). The matrix correction takes into

203   account oxygen calculated by cation stoichiometry and the oxygen equivalent from F. Cation

204   proportions (including reassignment of total Fe to Fe^{2+} and Fe^{3+}) and garnet end members were

205   calculated using the Excel spreadsheet written by Locock (2008).

206   We also report EPMA data for two samples (GRR732 and GRR1429) that were acquired

207   at Caltech using a JEOL JXA-8200. We used protocols for these analyses similar to those used at

208 UMN but did not measure F. Reference materials for calibration included synthetic pyrope for

209 Mg, Al, and Si; synthetic tephroite (GRR392) for Mn; synthetic fayalite for Fe; grossular

210 (GRR1386) for Ca; and synthetic rutile, Cr_2O_3, and V_2O_5 for Ti, Cr, and V, respectively.

211

212   **RESULTS**

213 **FTIR spectroscopy**

214   FTIR spectra representing the full variation in O-H stretching vibrations in the grossular

215 samples we studied are displayed in Figure 1. Following Rossman and Aines (1991), these

216 spectra can be separated into different classes according to the most prominent absorption bands

217 present. Class 2, represented by GRR42 (Fig. 1a), is dominated by strong peaks at 3647, 3656,

218 3676, and 3687 cm^{-1}, with the highest peak at 3647 cm^{-1}. A subset of spectral class 2 is class 2b,

219 which exhibits the same bands at high frequency (also with maximum absorbance at 3647 cm^{-1})

220 but has multiple bands between 3600 and 3500 cm^{-1} (Fig. 1a). Class 2b is represented by five of

221 the East African garnets (GRR229, GRR732, GRR771, GRR1386a, and GRR1386), which have

222 spectra with similar shapes but varying Abs_{tot} (Table 1 and supplemental Fig. S1). Three

223 grossular garnets (GRR1122, GRR1429, and GRR1756) fall into class 7 in the Rossman and

224 Aines scheme because their strongest absorption is at 3599 cm^{-1} rather than at 3647 cm^{-1}, but

225 otherwise their spectra are similar to class 2b; class 2b and class 7 are compared on the same

226 scale in Figure 1b.

227   The Asbestos garnet JLM83a (Fig. 1c) is typical of class 3, with a strong peak at 3631

228 cm^{-1} that is not as prominent in the other garnets. JLM83a also has bands centered at ~3621,

229 3644, 3659, 3665, 3677, and 3689 cm^{-1}. Garnets from Asbestos fall into both classes 3 and 4,

230 where class 4 is defined by having its strongest peak at 3621 cm^{-1}. Figure 1c compares spectra of

231   JLM83a to published spectra of some other Asbestos grossular garnets (GRR53 and GRR1537)

232   and end-member grossular crystals synthesized by Geiger and Armbruster (1997) and Withers et

233   al. (1998).

234   Whereas the absorbance among different East African grossular varies widely (Table 1

235   and supplemental Fig. S1), we failed to detect H zoning within any individual single crystal from

236   this area. The only crystals in our study that are significantly zoned, based on FTIR, are JLM83a

237   and GRR1429. Abs_{tot} in JLM83a varied by a factor of ~2 in the range between 3750 and 3300

238   cm^{-1}. All spectra have similar shapes, but relative intensities of the peaks at 3631 and 3621 cm^{-1}

239   vary (Fig. 1c). Rossman and Aines (1991) noted a comparable variation in Abs_{tot} for GRR53,

240   from the same locality. Systematic zoning patterns (such as core-rim relationships or sector

241   zoning) could not be deciphered in the randomly cut slab of JLM83a that we used for both FTIR

242   and SIMS measurements. Although variations in absorbance in Asbestos garnets have been

243   attributed previously to birefringence (Rossman and Aines 1986; Allen and Buseck 1988), our

244   SIMS measurements (Table 3 and discussion below) demonstrate that actual differences in H

245   concentration are a more important factor in this crystal.

246   GRR1429 is also birefringent, which might be the cause of the variations in Abs_{tot} (about

247   5% relative) in this sample. We used the average of seven baseline-corrected, unpolarized

248   spectra taken on separate spots to estimate its H_2O content.

249   Close examination of the spectrum of GRR1386 (Fig. 1a) reveals 12 peaks between 3700

250   and 3500 cm^{-1} and the shoulders on some of the bands indicate that curve fitting should take into

251   account more than 12 bands. Figure S5 in the supplementary material displays an example of

252   curve fitting for this garnet. We fit 15 bands with a pseudo-Voigt profile (mixed Gaussian and

253   Lorentzian), at 3531, 3539, 3546, 3567, 3583, 3599, 3608, 3623, 3631, 3643, 3647, 3657, 3664,

254   3674, and 3688 cm^{-1}. Although the fit is obviously non-unique, our peak positions (with initial

255   guesses based on visual examination) are within 1 cm^{-1} of those fit for the same sample by

256   Geiger and Rossman (2020a), with the slight difference that we fit an additional band at 3539

257   cm^{-1} not present in their fit. We used these peak positions as a basis to fit spectra for the other

258   grossular garnets. Fitted peak centers in other samples are mostly within 1 cm^{-1} of those for

259   GRR1386, with a few deviations up to 3 cm^{-1}. A table with the fit results for all samples is

260   provided in the supplementary material.

261   The cooling experiment conducted on GRR1386 demonstrates that nearly all the mid-IR

262   absorption in this garnet can be attributed to structurally incorporated O-H, with most bands

263   shifting to higher energies upon cooling to 77 K (Fig. 2). There is no evidence for band splitting

264   at low T, as observed in many other garnets (Geiger et al. 1991; Geiger and Rossman 2018).

265   However, enlargement of the baseline region reveals a broad absorption band at ~3400 cm^{-1} that

266   shifts to ~3240 cm^{-1}, typical of the transition from liquid water to ice (also plotted for

267   comparison in Fig. 2 are spectra for water and ice from Bertie and Lan 1996 and Johnson and

268   Rossman 2003). The 3400 cm^{-1} band is apparently also present in some of the other garnets, but

269   quantification is hampered by high-frequency interference fringes in most spectra (not visible at

270   the scales used in Fig. 1). The liquid water in GRR1386 is probably contained in sub-micrometer

271   sized fluid inclusions, as found in other NAMs (e.g., Johnson and Rossman 2003; Mosenfelder et

272   al. 2011). Its contribution to Abs_{tot} for this sample amounts to 1.2%. We have elected not to

273   correct any of the estimates for Abs_{tot} in Table 1 for the possible presence of H_2O. Furthermore,

274   we have ignored another possible contribution to Abs_{tot} in the O-H stretching region from the

275   lowest energy spin-allowed Fe^{2+} transition in grossular with FeO content greater than 1 wt%

276   (GRR42, GRR1122, GRR1386a, GRR1429, and JLM83a). This band should occur at lower

277   energy compared to other garnets (Geiger and Rossman 1994), because the larger size of the X

278   cation site in grossular leads to greater splitting of the Fe^{2+} bands (White and Moore 1972).

279   However, its exact position is difficult to determine owing to superposition of O-H stretching

280   vibrations (Slack and Chrenko 1971; White and Moore 1972).

281

282   **ERDA**

283   H_2O concentrations of the three grossular garnets, three rhyolitic glasses, and dry

284   forsterite as determined by ERDA are given in Table 2. ERDA and PIXE detector maps of the

285   analyzed areas for two of the garnets (GRR1756 and GRR732) revealed no significant

286   heterogeneities, but a small, anomalous region of interest with high H and Ca content in GRR771

287   was excluded in the calculation of its bulk H content. This "hot spot" probably represents surface

288   contamination (Withers et al. 2012). Bulk H (ERDA) and Ca (PIXE) maps for this sample are

289   provided in the supplementary material.

290   The nominal H_2O concentration measured by ERDA in GRR1017 forsterite, established

291   as an ultra-dry "blank" material with ≤ 0.007 µg/g H_2O (Mosenfelder et al. 2011), is 101±14

292   µg/g. The bulk H concentrations for grossular are strongly correlated with Abs_{tot} (Fig. 3). We

293   applied a York regression to the data (York et al. 2004; Vermeesch 2018), taking into account

294   uncertainties in both Abs_{tot} and the ERDA measurements. The regression yields an intercept of

295   100±13 µg/g H_2O, which is the value we subtract to arrive at the blank-corrected H_2O

296   concentrations. The slope of the fit line provides the following calibration for infrared

297   measurements:

298

299   C_{H_2O} (µg/g) $= 0.370 \, (\pm 0.035, 2\sigma) \times Abs_{tot}$ (1)

300

301   The integral molar absorption coefficient (ε_i, in L · mol^{-1} · cm^{-2}) can be derived by substituting

302   the above relation into a modified form of the Beer-Lambert law (e.g., Johnson and Rossman,

303   2004),

304

305   C_{H_2O} (μg/g) $= Abs_{tot} \times 18.015 \times 10^6/[\rho \cdot \varepsilon_i]$,   (2)

306

307   where ρ is the density of the mineral (in g/L, or kg/m^3). Assuming for simplicity a typical density

308   for V-bearing grossular of 3615 kg/m^3 (Maldener et al. 2003), we derive a value for ε_i of 13,470

309   L · mol^{-1} · cm^{-2}.

310   A check on the accuracy of our ERDA data on grossular is provided by the results on the

311   three rhyolitic glasses, which are in excellent agreement with previously published total H_2O

312   concentrations determined for these samples using Karl-Fischer titration (Tenner et al. 2009).

313   The H_2O contents of the glasses measured by ERDA are within 5% of the reference values.

314

315   **SIMS and EPMA measurements of H and F**

316   SIMS data for the sessions conducted in 2012 and 2016 are summarized in Table 3, with

317   complete data for all individual analyses provided in the supplementary material. Statistics are

318   reported in this paper using the symbology of Fitzsimons et al. (2000). Internal precision in

319    $^{16}OH/^{18}O$ (calculated from $2s_{\bar{x}}$, the standard error of the mean for 20 or 30 cycles through the

320   mass sequence) ranged from 0.24 to 1.35% relative for all garnets except GRR1122-HT (the

321   blank) and JLM83a. Measured $^{19}F/^{18}O$ ratios were similarly precise (0.15 to 0.52%). The high

322   variability in internal precision as well as external precision (reproducibility) for JLM83a is

323   discussed below.

324         $^{16}OH/^{18}O$ for each garnet with the exception of JLM83a is plotted in Figure 4 as a

325   function of H_2O concentration determined from FTIR data using the ERDA calibration. Similar

326   plots are derived if ^{30}Si is used instead of ^{18}O as the reference mass. Uncertainties in H_2O

327   concentration were estimated by propagating the error in Abs_{tot} (Table 1) and the uncertainty in

328   the fit to the ERDA data (Fig. 3 and Equation 1). York regressions applied to the data for East

329   African garnets (GRR229, GRR732, GRR771, GRR1386, GRR1386a, and/or GRR1756) have

330   indistinguishable slopes for the two sessions. These regressions also fit well to the data for

331   GRR1429 and GRR1122 measured in 2012. However, the 2016 data for GRR1122 are

332   significantly offset from the regression line, as are both the 2012 and 2016 data for GRR42.

333   In the case of GRR1122 we provisionally attribute this discrepancy to heterogeneity in

334   the sample not recognized from FTIR data and insufficiently probed by the six SIMS analyses

335   that were acquired. The heterogeneity could be related to the presence of fluid inclusions,

336   indicated by a weak broad band at 3420 cm^{-1} similar to that seen in GRR1386 (Fig. 2). As for

337   GRR42, the consistency in values for seven analyses from the two sessions suggests a different

338   explanation for the offset from the regression. In the discussion section, we explore the

339   possibility that the H concentration of GRR42 is significantly underestimated owing to the

340   frequency dependence of the IR molar absorption coefficient, which cannot be accurately

341   constrained from our ERDA data.

342   Fluorine concentrations measured by SIMS and EPMA are compared in supplemental

343   Figure S8. The SIMS concentration values are tied to our redetermination of reference values for

344   the F-bearing basaltic glasses we regularly use for calibration, not taking into account any

345   possible SIMS matrix effect. The close correspondence between SIMS and EPMA values (with

346   all values reasonably close to the 1:1 line) suggests that any such matrix effect is minimal in this

347   case.

348   The heterogeneity in apparent H_2O concentrations measured by FTIR in JLM83a was

349   confirmed by the grid map of SIMS analyses taken over approximately the same area (Fig. 5).

350   The SIMS analyses also reveal heterogeneity in F, which was additionally confirmed by EPMA

351   (see supplementary material). The measurements using SIMS, FTIR, and EPMA cannot be

352   compared directly to determine a zoning pattern because the FTIR analyses are taken in

353   transmission, whereas the SIMS and EPMA measurements sample a volume that is close to the

354   surface (~1-2 μm deep for SIMS, and ~3 μm deep for EPMA at the analytical conditions used).

355   However, the range in apparent H_2O concentrations measured by FTIR (256-571 μg/g) is similar

356   to the range measured by SIMS (170-576 μg/g), calculated by applying the York regression in

357   Figure 4b. For the sake of this comparison we discard four analyses (marked by asterisks in Fig.

358   5) that were affected by the spike in background contaminant levels in the vacuum caused by the

359   cold trap running out of liquid N_2 (see supplementary material). These analyses had $^{12}C/^{18}O$

360   ratios one to two orders of magnitude higher than the other analyses.

361   Following the 2012 session, it became apparent that ^{19}F and ^{16}OH are correlated for

362   some grossular garnets, particularly the East African samples with similar class 2b and class 7

363   FTIR spectra (Fig. 6a). A similar correlation was noted for spessartine (Fig. 6b). An even more

364   robust correlation exists for the data taken on JLM83a alone (Fig. 6a). The values in Figure 6a

365   for JLM83a represent average $^{16}OH/^{18}O$ and $^{19}F/^{18}O$ for each analysis. However, the internal

366   precision of the analyses varies widely, with $s_{\bar{x}}/\hat{s}_{\bar{x}}$ (where $\hat{s}_{\bar{x}}$ is the precision predicted by

367   Poisson statistics; Fitzsimons et al., 2000), ranging from 1 (ideal) to 30 (poor). We would

368   normally discriminate against SIMS measurements with such high $s_{\bar{x}}/\hat{s}_{\bar{x}}$ values; for instance, in

369   Mosenfelder et al. (2011) all analyses of olivine with $s_{\bar{x}}/\hat{s}_{\bar{x}} > 5$ were filtered out. High $s_{\bar{x}}/\hat{s}_{\bar{x}}$ in

370   olivine and orthopyroxene has been attributed to the presence of sub-micrometer to micrometer-

371   sized inclusions of hydrous minerals (such as serpentine and amphibole) and/or fluid inclusions

372   (Mosenfelder et al. 2011; Mosenfelder and Rossman 2013a). In the present case, however, we

373   attribute the high variability to zoning in H and F within the garnet itself. Analyses with high

374    $s_{\bar{x}}/\hat{s}_{\bar{x}}$ show strong cycle-to-cycle covariation between ^{19}F and ^{16}OH (Supplementary Fig. S8),

375   indicating that F and H are coupled on a sub-micrometer scale.

376

377   **DISCUSSION**

378   **Molar IR absorption coefficient for H_2O in grossular**

379   In Figure 7, we compare our ERDA data to H_2O concentrations measured (as a function

380   of Abs_{tot}) in grossular-rich garnets using other "absolute" techniques: NRA (Rossman and Aines

381   1991; Maldener et al. 2003), P_2O_5 cell coulometry using a moisture evolution analyzer (MEA,

382   Aines and Rossman 1984), H manometry (Aines and Rossman 1984), and continuous-flow mass

383   spectrometry (O'Leary et al., 2007). Also displayed in the graph is the regression line for all of

384   the data considered by Rossman and Aines (1991) for grossular and hydrogrossular with up to

385   12.75 wt% H_2O (with H_2O contents on the high end well-constrained using X-ray diffraction).

386   We have no definitive explanation for the discrepancy between H concentrations

387   measured in GRR732 by ERDA (599 μg/g H_2O) and continuous-flow mass spectrometry

388   (CFMS; 1062 μg/g H_2O); we can only speculate that the blank for that particular CFMS

389   measurement was higher than recognized. Our data show excellent agreement, however, with

390   some of the NRA data. In particular, the analyses by Maldener et al. (2003) on their TSAV (480

391 $\pm$ 40 $\mu g/g$ H_2O) and thin (0.0165 cm) slab of HESS1 (870 $\pm$ 90 $\mu g/g$ H_2O) samples lie close to

392 our regression line. These East African grossular garnets have IR spectra similar to those from

393 the same area that we measured with ERDA. Our data are in poorer agreement with Maldener et

394 al.'s analyses of a thicker (0.0312 cm) slab of HESS1 (950 $\pm$ 80 $\mu g/g$ H_2O) and with MALI (170

395 $\pm$ 20 $\mu g/g$ H_2O) and GRMALI (190 $\pm$ 20 $\mu g/g$ H_2O). The two NRA measurements of HESS1 are

396 in agreement with each other within mutual uncertainties, which suggests that there is a

397 discrepancy in the FTIR measurements (e.g., non-linearity of the detector for linear absorbance

398 higher than 1.5 in the thick HESS1 sample) or perhaps unrecognized H zoning in the crystal. The

399 discrepancies between our measurements and those on MALI and GRMALI might derive from

400 errors made in correcting the sample thicknesses for beam convergence in the microscope.

401 Furthermore, any inaccuracies in blank correction are also more likely to affect these low H

402 content samples.

403 The H concentrations of Asbestos grossular garnets GRR53 and GRR53F were measured

404 using three different techniques: H manometry, MEA, and NRA (Aines and Rossman 1984;

405 Rossman and Aines 1991). The poor agreement of our data fit with the values determined with

406 those techniques might be related to H zoning comparable to that in JLM83a. Hydrogen

407 manometry and MEA are bulk methods that sample a much larger volume than the FTIR

408 measurements and thus cannot account for fine-scale zoning. Even though NRA is a near-surface

409 technique, the beam size employed at that time was much larger (several mm) than the apparent

410 scale of H zoning in Asbestos grossular. Furthermore, the NRA measurement of GRR53F

411 employed a reaction with ^{19}F ions that was subsequently abandoned in favor of a more

412 reproducible reaction employing a ^{15}N beam (Rossman 2006).

413   There is a large discrepancy (Fig. 7) between our data fit on relatively low H content

414   grossular and the regression applied by Rossman and Aines (1991), which was largely

415   constrained by hydrogrossular garnets with high H contents. The discrepancy cannot be

416   attributed to the lower sample density of hydrogrossular; for instance, using Equation 2,

417   Crestmore hydrogrossular GRR1358, which has 12.75 wt% H_2O, Abs_{tot} of 158,750 cm^{-2}, and a

418   calculated density of 3050 kg/m^3 (Basso et al. 1983), would have an ε_i of 7354 L $\cdot$ mol^{-1} $\cdot$ cm^{-2},

419   lower than our new value by a factor of almost two. The data on hydrogrossular samples could

420   have been compromised by uncertainties in sample thickness or unrecognized H zoning, but

421   these factors are speculative and more work is needed to ascertain the reason for the large

422   apparent difference between low-H grossular and hydrogrossular.

423   The possibility of a difference in calibration factor for grossular and hydrogrossular was

424   already noted by Rossman and Aines (1991), and Rossman (2006) recommended a calibration

425   factor for low H content grossular of 0.14 (for absorbance in three directions). That value,

426   equivalent to 0.42 for the convention for Abs_{tot} used in this study, compares reasonably well to

427   our new value of 0.370 ±0.035 (Equation 1). We conclude that our new calibration is more

428   appropriate than the Rossman and Aines calibration for grossular with less than ~1 wt% H_2O.

429   Empirical and theoretical studies consistently show an increase in ε_i with decreasing

430   frequency for O-H absorption bands (Paterson 1982; Libowitzky and Rossman 1997; Balan et al.

431   2008; Mosenfelder et al., 2015). This means that an IR calibration based on grossular with

432   relatively low mean wavenumber might underestimate the H_2O contents of grossular with higher

433   mean wavenumber. Whereas our ERDA calibration was performed on grossular with mean

434   wavenumbers between 3595 and 3622 cm^{-1} (Table 1), GRR42 is dominated by bands with

435   significantly higher frequency (with a mean wavenumber of 3647 cm^{-1}; Fig. 1a, Table 1). A

436   frequency dependence to ε_i can therefore explain the offset of SIMS data for this sample in

437   Figure 4, but the magnitude of the dependence is poorly constrained. For the sake of calculating

438   formula units and garnet end-members (Table 4), we assume a H_2O concentration for this sample

439   based on the York regression shown in Figure 4a. Further work is needed to constrain the

440   frequency dependence of ε_i to determine whether this assumption is justified. Our calibration

441   also might underestimate H_2O concentrations for JLM83a and other Asbestos grossular garnets,

442   which also have a higher mean wavenumber (Table 1). Unfortunately, the zoning in some (or

443   all?) of these class 3 and 4 garnets will make this goal challenging, and class 2 garnets with

444   spectra like that of GRR42 are rare in our experience. A better way forward might entail

445   synthesizing grossular crystals at high P-T (Geiger and Armbruster 1997; Withers et al. 1998)

446   and establishing their homogeneity using a technique such as ERDA.

447

448   **Previous models of H and F incorporation mechanisms**

449   Hydrogen incorporation in garnets is classically assumed to take place via the

450   "hydrogarnet" substitution, whereby four H atoms bond to the O atoms surrounding a vacant Si

451   site. Hereafter, we refer to this substitution as $(4H)_{Si}^{\times}$, which is a commonly used, abbreviated

452   form of the following defect associate written in Kröger-Vink (1956) notation:

453

454   $\left\{ V_{Si}^{''''} - 4(OH)_O^{\cdot} \right\}^{\times}.$ (3)

455

456   Here, V represents a vacancy; the superscripts $^{\times}$, $^{\cdot}$ and $'$ represent null, positive, and negative

457   charges relative to the perfect structure, respectively; and the subscripts refer to Si and O

458   crystallographic sites. We recognize that some mineralogists might object to using point defect

459   symbolism to refer to both trace and high concentrations of elements, but we use it in the

460   following discussion for the sake of convenience.

461   The $(4H)_{Si}^{\times}$ mechanism is well established for H-rich garnets along the grossular-katoite

462   join (for review, see Beran and Libowitzky 2006; Grew et al. 2013; and Geiger and Rossman

463   2020a), not only from chemistry but from NMR, X-ray diffraction (XRD), and neutron

464   diffraction (Cohen-Addad et al. 1987; Lager et al. 1987, 1989; Cho et al. 1993). An analogous

465   substitution of four F atoms substituting for O surrounding a vacant Si site is well documented

466   for F-rich garnets, based on XRD (Smyth et al. 1990; Chakhmouradian et al. 2008) and negative

467   correlations between Si and F concentrations (Flohr and Ross 1989; Visser 1993;

468   Chakmouradian et al. 2008). This substitution can be written as:

469

470    $\left\{ V_{Si}^{''''} - 4(F)_O^{\cdot} \right\}^{\times}.$ (4)

471

472   This substitution differs structurally from $(4H)_{Si}^{\times}$ in the sense that F atoms can occupy the

473   regular site of O atoms, whereas the H atoms in $(4H)_{Si}^{\times}$ are bonded to O that is displaced from its

474   normal position owing to expansion of the tetrahedron (e.g. Lager et al. 1989).

475   Other substitution mechanisms for H and particularly for F in garnet have received

476   somewhat less attention. Valley et al. (1983) considered the possibility, in addition to

477   mechanisms (3) and (4), of F and H incorporation in grossular via the coupled substitution:

478

479    $(Al, Fe)^{3+} + O^{2-} \leftrightarrow (Mg, Fe)^{2+} + (F, OH)^{-} ,$ (5)
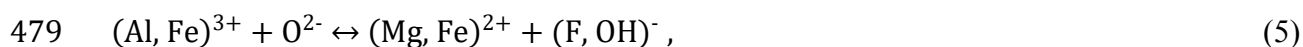
480

481   where the cations are located in the six-coordinated Y site. They recognized that verification of

482   this substitution relies on accurate determination of Fe^{2+}/Fe^{3+} as well as H and F content, beyond

483   the scope of their study. Various mechanisms involving coupled substitution of Ti and H have

484   also been considered, primarily for pyrope (Bell and Rossman 1992; Khomenko et al. 1994;

485   Geiger et al. 2000) but also for grossular (Reynes et al. 2020). Partial substitution of H for the Y-

486   cation in a hydrogrossular was inferred by Kalinichenko et al. (1987), based on NMR, and at

487   least two studies have inferred substitutions other than $(4H)^{\times}_{Si}$ in H-rich garnets based on crystal

488   chemical arguments (Birkett and Trcienski 1984; Basso and Cabella 1990). In principle OH^- or

489   F^- can replace O in the dodecahedral X-site in garnet, if it is vacant or contains a monovalent

490   cation (e.g., Andrut et al. 2002). For instance, a Ca vacancy in grossular can be compensated by

491   two H, which we notate as $(2H)^{\times}_{Ca}$. A similar substitution for the Y cation can be notated as

492    $(3H)^{\times}_{Al}$ or $(3H)^{\times}_{Fe}$, depending on the garnet composition.

493   Early on in the study of nominally anhydrous minerals it was recognized that the mid-IR

494   spectra of some garnets are incompatible with the $(4H)^{\times}_{Si}$ mechanism, because too many peaks

495   are present (Aines and Rossman 1984). The $(4H)^{\times}_{Si}$ substitution *sensu stricto* (cf. Geiger and

496   Rossman 2020a; see below) can result in a maximum of four O-H stretching vibrations, or two if

497   the symmetry of the garnet is maintained (Harmon et al. 1982; Aines and Rossman 1984). The

498   IR spectra of many pyrope, almandine, and andradite garnets are dominated by a broad,

499   asymmetric band that splits into two bands at low temperature (cooled by liquid N_2), thus

500   consistent with $(4H)^{\times}_{Si}$ (Geiger et al. 1991; Geiger and Rossman 2018). Differences in band

501   positions as a function of composition can be explained by the presence of different neighboring

502   X and Y cations, and the broad width of the bands can be explained by a combination of proton

503   disorder and variations in local cation configuration. On this basis, Geiger and Rossman (2018)

504   assigned bands at 3629, 3613, 3598, and 3563 cm^{-1} in pyrope, almandine, grossular, and

505   andradite respectively to $(4H)_{Si}^{\times}$. However, in grossular, as well as many spessartine garnets

506   (Aines and Rossman 1984; Arredondo et al. 2001) and some rare pyrope garnets from the Dora

507   Maira massif (Rossman et al. 1989), the multitude of sharp peaks cannot be explained by this

508   mechanism alone.

509   Additional constraints on H incorporation in grossular and garnets on the grossular-

510   andradite join come from experimental studies of H diffusion (Kurka et al. 2005;

511   Phichaikamjornwut et al. 2012; Reynes et al. 2018). All of these studies support the idea that

512   there are multiple sites for O-H incorporation, because various O-H bands decrease at different

513   rates during dehydration. In general, dehydration kinetics for bands at higher frequency have a

514   lower activation energy (E_a) than those at low frequency. For instance, Reynes et al. (2018)

515   measured E_a for a grossular-rich garnet in the range between 157 and 185 kJmol^{-1} for bands at

516   3628, 3645, 3657, and 3686 cm^{-1}, and in the range between 216 and 275 kJmol^{-1} for bands at

517   3533, 3576, and 3604 cm^{-1}. A positive dependence of the diffusion coefficient on f_{O_2} as well as

518   observations of color changes in sample rims in the experiments by Reynes et al. also support a

519   key role for Fe^{2+} in dehydration. Reynes et al. identify a fast diffusion mechanism, analogous to

520   that identified in many other nominally anhydrous minerals (Ingrin and Blanchard 2006), that is

521   limited by the availability of Fe^{2+}:

522

523    $M^{2+} + OH^{-} + \frac{1}{4}O_2 \rightarrow M^{3+} + O^{2-} + \frac{1}{2}H_2O,$ (6)

524
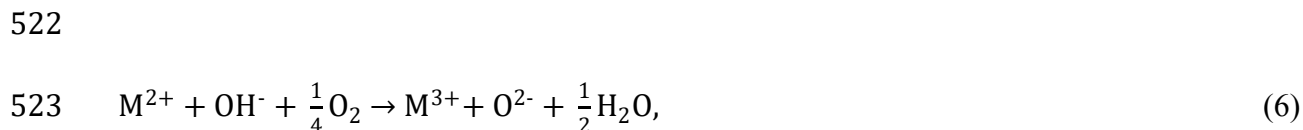
525   where M represents either Fe or Mn, which may or may not be directly tied to a defect

526   responsible for incorporating H. Our failed attempt to fully dehydrate GRR1122 (supplementary

527   Fig. S4) at low f_{O_2} (with virtually no change in spectra between dehydration steps 1 and 2) is

528   consistent with this interpretation. We will return to this point when we discuss our model for

529   coupled H-F substitution in the next section.

530   Another critical constraint on H incorporation in grossular comes from the study of Cho

531   and Rossman (1993), who performed solid-state ^{1}H NMR measurements on a synthetic end-

532   member katoite (Ca_3Al_2• $_3(OH)_{12}$) powder and single crystals of GRR1386 (Fig. 1a), GRR53

533   (Fig. 1c), and GRR1537 (Fig. 1c). From their analysis of multiple-quantum spectra, Cho and

534   Rossman concluded that the protons in katoite occur in closely spaced groups of four, as

535   expected for $(4H)_{Si}^{\times}$. However, the best fit to the multi-quantum spectrum of GRR1386 was for a

536   cluster size of two protons, and the best fit to the data for GRR1537 was for two separate clusters

537   consisting of two and four protons each. The class 4 IR spectrum of GRR1537 is dominated by a

538   band at 3621 cm^{-1} (Fig. 1c), which is the position of the main band in a synthetic hydrogrossular

539   with composition $Ca_3Al_2(SiO_4)_{2.28}(O_4H_4)_{0.72}$ (Rossman and Aines 1991). Therefore, Cho and

540   Rossman assigned this band to $(4H)_{Si}^{\times}$ and other, less intense bands to a different, unspecified

541   defect containing two closely spaced protons.

542   Geiger and Rossman (2020a, 2020b) offered a novel explanation for the sharp, high-

543   frequency bands in natural grossular. They hypothesized that bands at 3599, 3612, 3622, 3634,

544   and 3641 cm^{-1} correspond to clustered groups of $(4H)_{Si}^{\times}$ with cluster sizes of one, two, three, four

545   and five, respectively. A band at 3657 cm^{-1} was tentatively assigned to a cluster size of six, and a

546   band at 3660 cm^{-1} was assigned to a "finite size katoite cluster" based on the fact that the main

547   absorption in pure katoite (GRR1059; mislabeled as "Si 2.28" in Fig. 7 of Geiger and Rossman

548   2020a) occurs at this frequency (Rossman and Aines 1991). Bands at 3674 and 3688 cm^{-1} were

549   attributed to inclusions of hydrous minerals. This model explains all the features in IR spectra of

550   class 2, 3, and 4 grossular and all absorptions above ~3600 cm^{-1} in class 2b.

551   It is well known from studies of hydrous minerals that the strengths of O-H bonds (and

552   thus their vibrational frequencies) are affected by different cations sharing bonds with the same

553   O atom (i.e., second nearest neighbors to the H atom). For example, the frequencies of O-H

554   bonds in amphibole, which vary by up to ~50 cm^{-1}, can be reliably assigned to different cation

555   environments (e.g., Burns and Strens 1966). Recent work has also explored the effects of

556   neighboring cations on O-H stretching frequencies in olivine (Blanchard et al. 2017). The cluster

557   model of Geiger and Rossman (2020a,b), however, relies on an assumption that comparable

558   shifts in O-H bond frequencies are influenced by bonds in other $(4H)_{Si}^{\times}$ that are not directly

559   adjacent, because the tetrahedra in garnet are isolated from each other. Geiger and Rossman

560   justify this assumption as a consequence of the increase in Ca-O bond lengths between the end

561   members grossular (Geiger and Armbruster 1997) and katoite (Lager et al. 1987). It remains to

562   be shown by first-principles modeling or other methods whether or not this relaxation in Ca-O

563   distances for the end members also operates on a localized scale within small, isolated clusters of

564     $(4H)_{Si}^{\times}$ in garnets with trace amounts of H. It should also be noted that the model of Geiger and

565   Rossman ignores the results of Cho and Rossman (1993) that indicate some grossular garnets

566   contain a significant fraction of defects with only two protons. Furthermore, the assignment of

567   bands at 3674 and 3688 cm^{-1} to inclusions of hydrous phases is problematic, owing to geological

568   and spectroscopic reasons that we elaborate in the supplementary material. In the following

569   sections, we offer alternative explanations for some of the absorption bands that call on coupled

570   H and F substitution for Si as well as substitution of H (and possibly F) for cations in octahedral

571   and/or dodecahedral sites.

572

573 **Coupled substitution of H and F**

574   Our first clue that incorporation mechanisms of H and F in grossular might be entangled

575 came from correlations between ^{16}OH and ^{19}F in grossular (Fig. 6a) and spessartine (Fig. 6b),

576 prompting us to consider coupled substitution of H and F for Si (or other cations). While it is

577 possible that these correlations are coincidental and reflect nothing about coupled H-F

578 substitution, interpretation of the IR spectra combined with quantitative data on H and F

579 concentrations (Table 4) suggests otherwise.

580   Consider first the comparison between GRR42 and GRR1386: these crystals have the

581 same F content (0.25 wt%), but GRR1386 has nearly twice as much H_2O (0.13 wt%) as GRR42

582 (0.07 wt%; based on SIMS). The other obvious difference (Fig. 1a) is that both garnets have

583 significant absorbance above ~3620 cm^{-1}, but GRR42 has much lower absorbance at lower

584 frequencies. This suggests that some of the high-frequency bands are related to defects

585 containing both H and F, unless all F is bound in anhydrous defects (e.g., via Equation 4). We

586 draw a similar conclusion from the comparison between GRR732 and GRR1122 in Figure 1b:

587 these garnets have nearly the same H_2O content (0.052-0.054 wt%), but GRR732 has almost

588 twice as much F (0.11 wt%) as GRR1122 (0.06 wt%) and has stronger absorbance above ~3620

589 cm^{-1}, whereas GRR1122 has stronger absorbance at lower frequencies. Furthermore, the

590 strongest correlation between ^{16}OH and ^{19}F is evident in JLM83a, which has virtually no

591 absorbance at frequencies lower than ~3600 cm^{-1} (Fig. 1c) – again suggesting that the higher-

592 frequency O-H bands are related to F incorporation. An attempt to quantify these general

593 observations is summarized in Figure 8, where we plot F (per formula unit, Table 4) against the

594 band areas derived by spectral curve fitting for nine out of ten of the grossular garnets in the

595   study (JLM83a is excluded from this analysis because it is difficult to compare any given

596   spectrum to a precise F content in this zoned garnet).

597   Motivated partly by these observations and partly by the experiments and first-principles

598   density functional theory (DFT) calculations of Crépisson et al. (2014) on forsterite, we propose

599   that some of the bands at frequencies > 3600 cm^{-1} represent coupled H-F substitution for Si.

600   Following Cho and Rossman (1993) and Withers et al. (1998), we start with the assumption that

601   the band at 3621 cm^{-1}, with a shoulder at ~3610 cm^{-1}, represents $(4H)_{Si}^{\times}$. The asymmetry of the

602   stretching vibration in this region is consistent with the band structure in other garnet

603   compositions previously assigned to $(4H)_{Si}^{\times}$ (Geiger and Rossman 2018), although the bands in

604   grossular are narrower. Some or all of the bands at higher frequencies are then assigned to defect

605   associates involving both OH^{-} and F^{-}:

606

607    $\left\{ V_{Si}^{''''} - (OH)_{O}^{\cdot} - 3(F)_{O}^{\cdot} \right\}^{\times}$ (7)

608    $\left\{ V_{Si}^{''''} - 2(OH)_{O}^{\cdot} - 2(F)_{O}^{\cdot} \right\}^{\times}$ (8)

609    $\left\{ V_{Si}^{''''} - 3(OH)_{O}^{\cdot} - (F)_{O}^{\cdot} \right\}^{\times}$ (9)

610

611   Calculations made by Crépisson et al. (2014) indicate that some of these clumped OH-F

612   defects in forsterite lead to O-H vibrations at higher frequencies than those assigned by previous

613   studies to the $(4H)_{Si}^{\times}$ defect. For instance, the single O-H stretching vibration corresponding to

614   defect (7) is at 3674 cm^{-1}, as opposed to the four O-H vibrations predicted for the most stable

615    $(4H)_{Si}^{\times}$ configurations, which are between ~3400 and 3625 cm^{-1} (Balan et al. 2011; Umemoto et

616   al. 2011). In general, the frequencies of bands assigned to the various clumped OH-F defects

617   decrease as the number of F atoms decreases, but complexities arise owing to the three non-

618   equivalent crystallographic sites for O in the olivine structure. A positive frequency shift is also

619   predicted for a clumped OH-F defect in an octahedral site, compared to a fully protonated

620   vacancy. The positive O-H frequency shifts for sites where F^- replaces O^{2-} are presumably a

621   consequence of the influence of F^- (which is more electronegative than O^{2-}) on the geometry of

622   the polyhedron (Crépisson et al. 2014). The theoretically derived frequencies of the clumped

623   OH-F defects represented by Equations 7-9 are consistent with IR spectra of natural olivines

624   known to contain relatively high F concentrations (Sykes et al. 1994; Libowitzky and Beran

625   1995; Mosenfelder et al. 2011), which have bands at 3670, 3637, and 3620 cm^{-1} that are not

626   present in olivines with lower F contents.

627   Precise assignment of individual high-frequency bands in grossular to defects represented

628   by Equations 7-9 is difficult. We tentatively assign the band at 3687-3688 cm^{-1} to Equation (7),

629   by analogy to the corresponding defect in olivine. This attribution helps to reconcile the H

630   diffusion behavior observed by Kurka et al. (2005), who found that this band and the band at

631   3600 cm^{-1} decrease more rapidly than bands at 3645 and 3568 cm^{-1}. Specifically, H diffusion of

632   the defect associated with Equation 7 can take place rapidly via the reaction:

633

634     $$\left\{ V_{Si}^{''''} - (OH)_O^{\cdot} - 3(F)_O^{\cdot} \right\}^{\times} + Fe_{Ca}^{\times} + \frac{1}{4}O_2 = \left\{ V_{Si}^{''''} - (O)_O^{\times} - 3(F)_O^{\cdot} \right\}^{'} + Fe_{Ca}^{\cdot} + \frac{1}{2}H_2O. \quad (10)$$

635
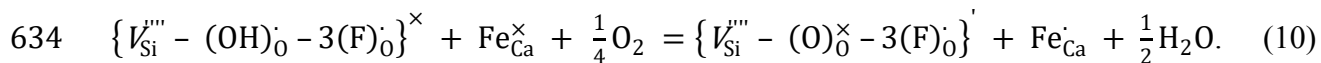
636   This reaction is similar to the generalized redox reaction represented by Equation (6) but is

637   defect-specific. In this case, F diffusion – which is inherently slower than H diffusion – is not

638   needed to maintain charge balance because dehydration involves oxidation of Fe^{2+} in the

639   dodecahedral site. Many studies have found that oxidation reactions of this type are faster than

640   reactions that require counter-diffusion of cations to maintain charge balance (Ingrin and

641   Blanchard 2006), and Reynes et al. (2018) provide direct evidence from color changes in

642   dehydrated crystals and experiments at variable f_{O_2} that oxidation of Fe^{2+} plays a key role in

643   dehydration of grossular.

644   The effect of dilute F substitution on local symmetry of the grossular structure is

645   unknown, so it is not straightforward to use group theory to predict how many bands should be

646   present for defects containing more than one O-H bond (Equations 8 and 9). Significant

647   proportions of cations other than Ca and Al in neighboring X and Y sites, such as V or Fe

648   (present in some of the grossular garnets in this study; Table 4), could also shift the frequencies

649   of the O-H bands, because these frequencies largely depend on the masses, ionic radii, and

650   electronic states of the neighboring cations (Burns and Strens 1966; Berry et al. 2007; Geiger and

651   Rossman 2018, 2020a). This effect is likely to be minor but may explain the small shifts up to 3

652   cm^{-1} for some peaks in our curve fits for different grossular spectra. The imperfect correlation of

653   F to the integrated absorbance of the high-frequency bands (Fig. 8a) could be related to the

654   additional presence of F in sites with no OH (e.g., Equation 4), vagaries of the fitting exercise, or

655   perhaps other mechanisms completely unrelated to F – such as the cluster model of Geiger and

656   Rossman (2020a,b) or coupled substitution of H and Ti (Reynes et al. 2020), which we discuss

657   below. Therefore, more work including ab initio calculations is needed to verify our hypothesis

658   that clumped OH-F defects are present in grossular. One attractive feature of our model is that

659   the presence of a significant proportion of defect (8) could partially explain the finding of Cho

660   and Rossman (1993) that H is predominantly present in clusters of two closely spaced protons in

661   GRR1386, and by extension to other class 2b grossular garnets.

662

663   **Low frequency O-H absorption bands**

664   No study has yet offered a satisfactory explanation for all the bands below ~3600 cm^{-1} in

665   class 2a and class 7 grossular (some of the bands are also present in class 5 and 6 grossular;

666   Rossman and Aines 1991). Geiger and Rossman (2020a) assigned the band at 3563 cm^{-1} to a

667   localized "hydroandradite group" consisting of a single $(4H)^{\times}_{Si}$ adjacent to Fe^{3+} in the octahedral

668   site, based on comparison to the most intense O-H band frequency in andradite IR spectra

669   (Amthauer and Rossman 1998; Geiger and Rossman 2018). Furthermore, they speculated that

670   their model for hydrogrossular clusters could be extended to assign other bands at 3581 and 3594

671   cm^{-1} to different sized hydroandradite clusters. This hypothesis is difficult to assess because the

672   total Fe content in many grossular garnets is too low to accurately determine Fe^{2+}/Fe^{3+} using

673   established methods. Our cation assignments (Table 4) based on stoichiometry using the

674   calculation scheme of Locock (2008) indicate that all of the Fe is Fe^{2+} for our garnets with 0.06

675   to 1.8 wt% FeO, but this method for calculating Fe^{2+}/Fe^{3+} suffers from considerable uncertainty

676   and Fe^{3+} may also be present.

677   The role of Ti in H incorporation in grossular and andradite was recently studied by

678   Reynes et al. (2020). They proposed coupled substitution of Ti on the Y site and 2H for Si, as

679   follows:

680

681    $\left\{ V^{''''}_{Si} - 2(OH)^{\cdot}_{O} \right\}^{''} + 2Ti^{\cdot}_{Al,Fe}$ (11)

682

683   FTIR spectra of the grossular studied by Reynes et al. are unusual compared to most grossular

684   garnets surveyed by Rossman and Aines (1991), containing only three bands at 3546, 3595, and

685   3652 cm^{-1}; the closest match is to GRR1359, a grossular from a metarodingite in the Gruppo di

686   Voltri, Italy (probably from a similar geologic setting as the rodingite grossular studied by

687   Reynes et al.). Bands at similar frequencies are also present in spectra of the class 2b grossular

688   samples in this study, centered at 3546, 3599, and 3657 cm^{-1} in GRR1386. Therefore, this

689   mechanism may also be important in these garnets, which contain between 0.3 to 0.6 wt% TiO$_2$

690   (Table 4). The presence of a band at 3652-3657 cm^{-1} related to defect (11) could also partially

691   explain the imperfect correlation of F content to high frequency absorption in Figure 8a.

692   Another possibility is that some of the low frequency bands represent H substitution in

693   dodecahedral and/or octahedral sites via defects such as $(2H)^{\times}_{Ca}$ or $(3H)^{\times}_{Al}$, respectively. This

694   attribution could further help to explain the identification of two-proton clusters in GRR1386 by

695   Cho and Rossman (1993), if a large fraction of the H is located in the defects (8), (11), and

696    $(2H)^{\times}_{Ca}$ combined. Substitution of H via defects such as $(2H)^{\times}_{Ca}$ would also be consistent with

697   the higher E_a measured for lower frequency O-H bands by Reynes et al. (2018), if dehydration

698   requires counter-diffusion of Ca to take place (as opposed to dehydration via a fast-redox

699   mechanism). Although this hypothesis is highly speculative, DFT calculations for nominally

700   anhydrous minerals to date indicate that the $(4H)^{\times}_{Si}$ defect gives rise to O-H absorptions at higher

701   frequencies than substitutions involving octahedral cation vacancies. This phenomenon applies

702   to olivine (Balan et al. 2011; Umemoto et al. 2011), enstatite (Balan et al. 2013), wadsleyite

703   (Blanchard et al. 2013), and ringwoodite (Blanchard et al. 2009).

704   In principle, clumped OH-F defects in octahedral or dodecahedral sites are also possible,

705   as are coupled substitution mechanisms like those put forth by Valley et al. (1983) (Equation 5).

706   The intensity of the low-frequency bands in East African grossular also correlates positively with

707   F content (Fig. 8b). By analogy to our argument with the high frequency bands, this might

708   suggest a role for such defects in addition to clumped OH-F in tetrahedral sites. One weakness

709   with this idea is that the presence of isolated, clumped OH-F defects in octahedral or

710 dodecahedral sites would require the presence of Si-F bonds, because all O sites in the garnet

711 structure are shared between the tetrahedral site, two dodecahedral sites, and the octahedral site.

712 As noted by Smyth et al. (1990), there are no known mineral structures in which F bonds directly

713 to tetrahedral Si. However, some NMR studies provide evidence for Si-F bonding in

714 aluminosilicate glasses (e.g., Zeng and Stebbins 2000; Liu and Nekvasil 2002). It is probably

715 more likely that any defect associate involving clumped OH-F in an octahedral or dodecahedral

716 site would be paired with a neighboring defect associate in the tetrahedral site (e.g., three H and

717 one F substituting for Si).

718

719 **Coupled H and F substitution in other garnet compositions**

720   Our model of coupled H and F substitution for Si in grossular likely applies to garnets

721 with other compositions. Data from our 2012 session show strong correlations between ^{16}OH and

722 ^{19}F in 11 spessartine garnets (Fig. 6b), similar to the correlations seen for East African grossular

723 (Fig. 6a). These spessartine garnets have peaks at ~3582, 3595, 3615, 3625, 3640, and 3649 cm^{-1}

724 (Arredondo et al. 2001). Bands at similar frequencies are also present in spectra of a spessartine

725 with up to 3.8 wt% F studied by Smyth et al. (1990). Aines and Rossman (1984) recognized that

726 these six peaks (which can be fit with even more bands) cannot be explained by $(4H)_{Si}^{\times}$ alone. It

727 is tempting to assign the band at 3595 cm^{-1} (with a shoulder at 3582 cm^{-1}) to $(4H)_{Si}^{\times}$. The lower

728 frequency compared to katoite or grossular can be explained by the high mass of Mn^{2+}

729 (compared to Ca^{2+}) in the X-site (Geiger and Rossman 2018). However, relative peak heights at

730 3582 and 3595 cm^{-1} vary considerably in garnets from different parts of the pegmatite and in

731 spessartine from the Himalayan Mine (Arredondo et al. 2001), which is not easily reconcilable

732 with a single O-H site being responsible for both bands. Taken together, these observations

733   suggest the possibility that some or all of the bands represent clumped OH-F defects analogous

734   to those we propose for grossular.

735   The presence of high frequency bands in some garnets along the grossular-andradite join

736   (Phichaikamjornwut et al. 2012; Geiger and Rossman 2020a) was already noted. In the

737   supplementary material, we provide IR spectra of a $Grs_{26}Adr_{74}$ garnet (GRR1830) and a nearly

738   end-member andradite (GRR2103) that we analyzed by SIMS in 2012. GRR1830 has at least

739   eight bands, with peaks at 3560, 3580, 3589, 3617, 3640, 3653, 3660, and 3677 cm^{-1}. The band

740   locations are similar to those in the garnets from Thailand studied by Phichaikamjornwut et al.

741   (2012). The spectrum of GRR2103 is dominated by a strong peak at 3563 cm^{-1} (with a shoulder

742   at about 3547 cm^{-1}) and has only weak absorbance above 3600 cm^{-1}. Published spectra of other

743   garnets close to end-member andradite also typically do not have these bands (e.g., Amthauer

744   and Rossman 1998; Geiger and Rossman 2018). However, Amthauer and Rossman (1998) noted

745   spectral complexity in a near-end member andradite from Stanley Butte, AZ, USA (GRR1137).

746   Again, the number of bands in GRR1830 and the grossular-andradite garnets studied by

747   Phichaikamjornwut et al. (2012) raises the possibility that some of them represent clumped OH-F

748   defects. This inference is also consistent with SIMS data. Whereas GRR1830 yielded an average

749    $^{19}F/^{18}O$ ratio of 0.191, equivalent to 76 $\mu g/g$ F, measurements during the same session on

750   GRR2103 yielded $^{19}F/^{18}O$ ratios just barely above the detection limit (<1 $\mu g/g$ F; Mosenfelder

751   and Rossman 2013a).

752   Coupled H-F substitution is less likely to be important in pyrope, if only because it

753   typically contains significantly lower concentrations of both elements compared to other garnet

754   compositions. Mosenfelder and Rossman (2012) report 0.2 to 10 $\mu g/g$ F in pyrope garnets from

755   mantle xenoliths that contain up to 135 $\mu g/g$ H_2O (using the IR calibration of Bell et al. 1995).

756   These xenoliths also contain other phases (olivine, orthopyroxene, and/or clinopyroxene) that

757   can partition much of the available F (Mosenfelder et al. 2011; Mosenfelder and Rossman

758   2013a,b). Nearly end-member pyrope from the Dora Maira massif represents an unusual case; its

759   IR spectra are unlike those of other pyrope-almandine garnets, with sharp peaks at 3602, 3641,

760   3651, and 3662 cm^{-1} (Rossman et al. 1989). As noted above similar bands are present in a pyrope

761   synthesized by Geiger et al. (1991).

762   On the one hand, Lu and Keppler (1997) attributed the bands in Dora Maira pyrope to O-

763   H defects associated with Li and B substitution, based on Li_2O and B_2O_3 concentrations

764   measured by ICP-AES (inductively coupled plasma atomic emission spectroscopy). On the other

765   hand, our attribution of high-frequency bands to clumped OH-F defects is particularly apropos in

766   this case because some Dora Maira garnets contain inclusions of phlogopite with up to 1.6 wt%

767   F as well as other F- and Cl-bearing phases, unequivocally indicating that they formed in a

768   halogen-rich environment (Philippot et al. 1995). Furthermore, SIMS analyses of Dora Maira

769   pyrope by Tenner et al. (2009) – while uncalibrated for F concentration – yielded a $^{19}F/^{30}Si$ ratio

770   of 0.215, approximately one order of magnitude higher than ratios measured in pyrope garnets

771   from mantle xenoliths (0.008-0.025). A rough estimate of 30 μg/g F can be derived by

772   comparing to our SIMS data on pyrope (Mosenfelder and Rossman 2012), including MON9

773   from Bell et al. (1995), which was also measured by Tenner et al.

774

775   **IMPLICATIONS**

776   This work highlights technical advances in analytical methods for F and H that could

777   facilitate future studies using garnets to constrain the activities of H_2O and F-species in fluids in

778   equilibrium with garnet-bearing phase assemblages. The present study – including our new

779   calibration for the IR molar absorption coefficient in grossular – most directly applies to geologic

780   problems in the Earth's crust. However, measurements of trace F and H in garnets from mantle

781   xenoliths may also provide additional constraints on recycling of these elements into the mantle,

782   already a topic of interest addressed by studies of F and H in olivines and pyroxenes.

783   Fine-scale zoning of H in garnets such as those from Asbestos or the garnets studied by

784   Jamtveit and Hervig (1994) or Reynes et al. (2020) is probably best studied using micro-

785   analytical techniques such as SIMS or FTIR conducted with a focal plane array (FPA) detector,

786   which is becoming more widely available (the FPA detector has a higher spatial resolution than

787   normal MCT detectors such as those we used; e.g., Reynes et al. 2020). We have also

788   demonstrated that F can be measured reliably with EPMA at levels down to ~50 μg/g, and it

789   should be possible to achieve higher analytical throughput at lower cost with EPMA compared to

790   SIMS. Furthermore, in principle, minimum estimates for F concentrations in garnet could be

791   constrained from FTIR spectra alone, once band assignments for coupled H-F defects are

792   confirmed and controversy over incorporation mechanisms is settled. We expect that theoretical

793   calculations will shed additional light on coupled H-F substitution in garnets and other nominally

794   anhydrous minerals.

795

805

REFERENCES

807   Aines, R.D., and Rossman, G.R. (1984) The hydrous component in garnets: pyralspites.

808   American Mineralogist, 69, 116-1126.

809   Allen, F.M., and Buseck, P.R. (1988) XRD, FTIR, and TEM studies of optically anisotropic

810   grossular garnets. American Mineralogist, 73, 568-584.

811   Amthauer, G., and Rossman, G.R. (1998) The hydrous component in andradite garnet. American

812   Mineralogist, 83, 835–840.

813   Andrut, M., Wildner, M., and Beran, A. (2002) The crystal chemistry of birefringent natural

814   uvarovites. Part IV. OH defect incorporation mechanisms in non-cubic garnets derived

815   from polarized IR spectroscopy. European Journal of Mineralogy, 14, 1019–1026.

816   Armstrong, J.T. (1988) Quantitative analysis of silicate and oxide minerals, comparison of

817   Monte Carlo, ZAF and $\phi(\rho z)$ procedures. In D.E. Newbury, Ed. Microbeam analysis, p.

818   239-246. San Francisco Press, San Francisco, CA.

819   Arredondo, E.H., Rossman, G.R., and Lumpkin, G.R. (2001) Hydrogen in spessartine-almandine

820   garnets as a tracer of granitic pegmatite evolution. American Mineralogist, 86, 485-490.

821   Aubaud, C., Withers, A.C., Hirschmann, M., Guan, Y., Leshin, L.A., Mackwell, S., and Bell,

822   D.R. (2007) Intercalibration of FTIR and SIMS for hydrogen measurements in glasses

823   and nominally anhydrous minerals. American Mineralogist, 92, 811-828.

824 Balan, E., Refson, K., Blanchard, M., Delattre, S., Lazzeri, M., Ingrin, J., Mauri, F., Wright, K.,

825   and Winkler, B. (2008) Theoretical infrared absorption coefficient of OH groups in

826   minerals. American Mineralogist, 93, 950-953.

827 Balan, E., Ingrin, J., Delattre, S., Kovacs, I., and Blanchard, M. (2011) Theoretical infrared

828   spectrum of OH-defects in forsterite. European Journal of Mineralogy, 23, 285–292.

829 Basso, R., Giusta, A.D., and Zefiro, L. (1983) Crystal structure refinement of plazolite: a highly

830   hydrated natural hydrogrossular. Neues Jahrbuch für Mineralogie Monatshefte, H.6, 251-

831   258.

832 Basso, R., and Cabella, R. (1990) Crystal chemical study of garnets from metarodingites in the

833   Voltri Group metaophilites (Ligurian Alps, Italy). Neues Jahrbuch für Mineralogie

834   Monatshefte, H.3, 127-136.

835 Bell, D. R., and Rossman, G. R. (1992) The distribution of hydroxyl in garnets from the sub-

836   continental mantle of southern Africa. Contributions to Mineralogy and Petrology, 111,

837   161-178.

838 Bell, D.R., Ihinger, P.D., and Rossman, G.R. (1995) Quantitative analysis of trace OH in garnet

839   and pyroxene. American Mineralogist, 80, 465–474.

840 Beran, A., and Libowitzky, E. (2006) Water in natural mantle minerals II: olivine, garnet, and

841   accessory minerals. In H. Keppler and J. R. Smyth, Eds., Water in Nominally Anhydrous

842   Minerals, 62, p. 169-191. Reviews in Mineralogy and Geochemistry, Mineralogical

843   Society of America, Chantilly, Virginia.

844 Bernini, D., Wiedenbeck, M., Dolejs, D., and Keppler, H. (2012) Partitioning of halogens

845   between mantle minerals and aqueous fluids: implications for the fluid flow regime in

846   subduction zones. Contributions to Mineralogy and Petrology, 165, 117-128.

847   Berry, A., O'Neill, H.St.C., Hermann, J., and Scott, D.R. (2007) The infrared signature of water

848   associated with trivalent cations in olivine. Earth and Planetary Science Letters, 261,

849   134–142.

850   Bertie, J.E., and Lan, Z. (1996) Infrared intensities of liquids XX: the intensity of the OH

851   stretching band of liquid water revisited, and the best current values of the optical

852   constants of H_2O(I) at 25 °C between 15,000 and 1 cm^{-1}. Applied Spectroscopy 50, 1047-

853   1057. □□□□□□□□□

854   Beyer, C., Klemme, S., Wiedenbeck, M., Stracke, A., and Vollmer, C. (2012) Fluorine in

855   nominally fluorine-free mantle minerals: Experimental partitioning of F between olivine,

856   orthopyroxene and silicate melts with implications for magmatic processes. Earth and

857   Planetary Science Letters, 337-338, 1-9.

858   Birkett, T.C., and Trzcienski, W.E. (1984) Hydrogarnet: multi-site hydrogen occupancy in the

859   garnet structure. Canadian Mineralogist, 22, 675-680.

860   Blanchard, M., Balan, E., and Wright, K. (2009) Incorporation of water in iron-free ringwoodite:

861   a first-principles study. American Mineralogist, 94, 83–89.

862   Blanchard, M., Roberge, M., Balan, E., Fiquet, G., and Bureau, H. (2013) Infrared signatures of

863   OH defects in wadsleyite: A first-principles study. American Mineralogist, 98, 2132–

864   2143.

865   Blanchard M., Ingrin J., Balan E., Kovács I., and Withers A.C. (2017) Effect of iron and trivalent

866   cations on OH defects in olivine. American Mineralogist, 102, 302-311.

867   Burdo, R.A., and Morrison, G.H. (1971) Table of atomic and molecular lines for spark source

868   mass spectrometry of complex sample-graphite mixes. Report no. 1670. Materials

869   Science Center, Cornell University, Ithaca, New York.

870   Bureau, H., Raepsaet, C., Khodja, H., Carraro, A., and Aubaud, C. (2009) Determination of

871   hydrogen content in geological samples using elastic recoil detection analysis (ERDA).

872   Geochimica et Cosmochimica Acta 73, 3311–3322.

873   Burns, R.G., and Strens R.G.J. (1966) Infrared study of the hydroxyl bands in clinoamphiboles.

874   Science, 153, 890-892

875   Chakhmouradian, A.R., Cooper, M.A., Medici, L., Hawthorne, F.C., and Adar, F. (2008)

876   Fluorine-rich hibschite from silicocarbonatite, Afrikanda complex, Russia: crystal

877   chemistry and conditions of crystallization. Canadian Mineralogist, 46, 1033-1042.

878   Chantler, C.T., Olsen, K., Dragoset, R.A., Chang, J., Kishore, A.R., Kotochigova, S.A., and

879   Zucker, D.S. (2005) X-Ray Form Factor, Attenuation and Scattering Tables (version 2.1).

880   [Online] Available: http://physics.nist.gov/ffast. National Institute of Standards and

881   Technology, Gaithersburg, MD.

882   Cho, H., and Rossman, G.R. (1993) Single-crystal NMR studies of low-concentration hydrous

883   species in minerals: grossular garnet. American Mineralogist, 78, 1149-1164.

884   Cohen-Addad, C., Ducros, P., and Bertaut, E.F. (1967) Étude de la substitution du groupement

885   SiO_4 par (OH)4 dans les composés $Al_2Ca_3(OH)_{12}$ et $Al_2Ca_3(SiO4)_{2.16}(OH)_{3.36}$ de type

886   grenat. Acta Crystallographica, 23, 220–230.

887   Crépisson, C., Blanchard, M., Bureau, H., Sanloup, C., Withers, A.C., Khodja, H., Surble, S.,

888   Raepsaet, C., Beneut, K., Leroy, C., Giura, P., and Balan, E. (2014) Clumped fluoride-

889   hydroxyl defects in forsterite: implications for the upper-mantle. Earth and Planetary

890   Science Letters, 390, 287–295.

891   Dalou, C., Koga, K.T., Shimizu, N., Boulon, J., and Devidal, J.L. (2012) Experimental

892   determination of F and Cl partitioning between lherzolite and basaltic melt. Contributions

893   to Mineralogy and Petrology, 163, 591-609.

894   Donovan, J.J., Lowers, H.A., and Rusk, B.G. (2011) Improved electron probe microanalysis of

895   trace elements in quartz. American Mineralogist, 96, 274-282.

896   Fitzsimons, I.C.W., Harte, B., and Clark, R.M. (2000) SIMS stable isotope measurement:

897   counting statistics and analytical precision. Mineralogical Magazine, 64, 59–83.

898   Flohr, M.J.K., and Ross, M. (1989) Alkaline igneous rocks of Magnet Cove, Arkansas:

899   metasomatized ijolite xenoliths from Diamond Jo quarry. American Mineralogist, 74,

900   113-131.

901   Geiger, C.A., and Armbruster, T. (1997) $Mn_3Al_2Si_3O_{12}$ spessartine and $Ca_3Al_2Si_3O_{12}$ grossular

902   garnet: dynamical structural and thermodynamic properties. American Mineralogist, 82,

903   740–747.

904   Geiger, C.A., and Rossman, G.R. (1994) Crystal field stabilization energies of almandine-pyrope

905   and almandine-spessartine garnets determined by FTIR near infrared measurements.

906   Physics and Chemistry of Minerals, 21, 516-525.

907   Geiger, C.A., and Rossman, G.R. (2018) IR spectroscopy and OH- in silicate garnet: the long

908   quest to document the hydrogarnet substitution. American Mineralogist, 103, 384-393.

909   Geiger, C.A., and Rossman, G.R. (2020a) Micro- and nano-size hydrogarnet clusters and proton

910   ordering in calcium silicate garnet: Part I. The quest to understand the nature of "water"

911   in garnet continues. American Mineralogist, 105, 455-467.

912   Geiger, C.A., and Rossman, G.R. (2020b) Micro- and nano-size hydrogarnet clusters in calcium

913   silicate garnet: Part II. Mineralogical, petrological, and geochemical aspects. American

914   Mineralogist, 105, 468-478.

915   Geiger, C.A., Langer, K., Bell, D.R., Rossman, G.R., and Winkler, B. (1991) The hydroxide

916   component in synthetic pyrope. American Mineralogist, 76, 49–59.

917   Geiger, C.A., Stahl, A., and Rossman, G.R. (2000) Single-crystal IR- and UV/ VIS-spectroscopic

918   measurements on transition-metal-bearing pyrope: The incorporation of hydroxide in

919   garnet. European Journal of Mineralogy, 12, 259–271.

920   Giuliani, G., Ohnenstetter, D., Palhol, F., Feneyrol, J., Boutroy, E., de Boissezon, H., and

921   Lhomme, T. (2008) Karelianite and vanadian phlogopite from the Merelani Hills gem

922   zoisite deposits, Tanzania. Canadian Mineralogist, 46, 1183-1194.

923   Giuliani, G., Fallick, A.E., Feneyrol, J., Ohnenstetter, D., Pardieu, V., and Saul, M. (2011)

924        $^{18}O/^{16}O$ and V/Cr ratios in gem tsavorites from the Neoproterozoic Mozambique

925   metamorphic belt: a clue towards their origins? Mineralium Deposita, 46, 671-676.

926   Grew, E., Locock, A.J., Mills, S.J., Galuskina, I.O., Galuskin, E.V., and Hålenius, U. (2013)

927   Nomenclature of the garnet supergroup. American Mineralogist, 98, 785-811.

928   Grützner, T., Kohn, S.C. Bromiley, D.W., Rohrbach, A., Berndt, J., and Klemme, S. (2017) The

929   storage capacity of fluorine in olivine and pyroxene under upper mantle conditions.

930   Geochimica et Cosmochimica Acta, 208, 160–170.

931   Guggino, S.N., and Hervig, R.L. (2011) Synthesis and characterization of five new F-bearing

932   basalt reference materials (Fba glasses): quantifying the fluorine content of the basaltic

933   glass standards BCR-2G, BHVO-2G, GSA-1G, GSC-1G, GSD-1G, GSE-1G, ML3B-G,

41

934   KL2-G, and ALV-519-4. American Geophysical Union, Fall Meeting 2011, abstract

935   #V31C-2535.

936   Harmon, K.M., Gabriele, J.M., and Nuttal, A.S. (1982) Hydrogen bonding in the tetrahedral

937     $O_4H_4^{4-}$ cluster in hydrogrossular. Journal of Molecular Structure, 82, 213–219.

938   Hauri, E.H., Wang, J., Dixon, J.E.,, King, P.L., Mandeville, C., and Newman, S. (2002) SIMS

939   analysis of volatiles in silicate glasses 1. Calibration, matrix effects and comparisons with

940   FTIR. Chemical Geology, 183, 99-114.

941   Hervig, R.L., and Bell, D.R. (2005) Fluorine and hydrogen in mantle megacrysts. American

942   Geophysical Union, Fall Meeting 2005, abstract V41A-1426.

943   Ingrin, J., and Blanchard, M. (2006) Diffusion of hydrogen in minerals. In H. Keppler and J.R.

944   Smyth, Eds., Water in Nominally Anhydrous Minerals, 62, p. 291–320, Reviews in

945   Mineralogy and Geochemistry, Mineralogical Society of America, Chantilly, Virginia.

946   Jamtveit, B., and Hervig, R.L. (1994) Constraints on transport and kinetics in hydrothermal

947   systems from zoned garnet crystals. Science, 263, 505-508.

948   Johnson E. A., and Rossman G. R. (2003) The concentration and speciation of hydrogen in

949   feldspars using FTIR and ^{1}H MAS NMR spectroscopy. American Mineralogist, 88, 901–

950   911.

951   Johnson E. A., and Rossman G. R. (2004) A survey of hydrous species and concentrations in

952   igneous feldspars. American Mineralogist, 89, 586–600.

953   Kalinichenko, A.M, Proshko, Y.Ya, Matyash, LV., Pavlishin, V.L, and Gamarnik, M.Ya. (1987)

954   Geochemistry international, 24, 132-135.

955   Khomenko, V.M., Langer, K., Beran, A., Koch-Mü ler, M., and Fehr, T. (1994) Titanium

956   substitution and OH-bearing defects in hydrothermally grown pyrope crystals. Physics

957   and Chemistry of Minerals, 20, 483-488.

958   Klemme, S., and Stalder, R. (2018) Halogens in the Earth's mantle: what we know and what we

959   don't. In D.E. Harlov and L. Aranovich, Eds., The Role of Halogens in Terrestrial and

960   Extraterrestrial Geochemical Processes, p. 847-869. Springer, Cham, Switzerland.

961   Koga, K., Hauri, E., Hirschmann, M.M., and Bell, D. (2003) Hydrogen concentration analyses

962   using SIMS and FTIR: comparison and calibration for nominally anhydrous minerals.

963   Geochemistry, Geophysics, and Geosystems, 4, doi: 10.1029/2002GC000378.

964   Kröger, F., and Vink, H. (1956) Relations between the concentrations of imperfections in

965   crystalline solids. In F. Seitz and D. Turnbull, Eds., Solid state physics, 3. Elsevier,

966   Amsterdam, pp. 307-435.

967   Kurka, A., Blanchard, M., and Ingrin, J. (2005) Kinetics of hydrogen extraction and deuteration

968   in grossular. Mineralogical Magazine, 69, 359–371.

969   Lager, G.A., Armbruster, T., and Faber, G. (1987) Neutron and X-ray diffraction study of

970   hydrogarnet $Ca_3Al_2(O_4H_4)_3$. American Mineralogist, 72, 756–765.

971   Lager, G.A., Armbruster, T., Rotella, F.J., and Rossman G.R. (1989) OH substitution in garnets:

972   X-ray and neutron diffraction, infrared, and geometric-modeling studies. American

973   Mineralogist 74, 840–851.

974   Libowitzky, E., and Beran, A. (1995) OH defects in forsterite. Physics and Chemistry of

975   Minerals, 22, 387–392.

976   Libowitzky, E., and Rossman, G.R. (1997) An IR absorption calibration for water in minerals.

977   American Mineralogist, 82, 1111-1115.

978   Liu, Y., and Nekvasil, H. (2002) Si-F bonding in aluminosilicate glasses: Inferences from ab

979   initio NMR calculations. American Mineralogist, 87, 339-346.

980   Locock, A.J. (2008) An excel spreadsheet to recast analyses of garnet into end-member

981   components, and a synopsis of the crystal chemistry of natural silicate garnets.

982   Computers and Geosciences, 34, 1769-1780.

983   Lu, R., and Keppler, H. (1997) Water solubility in pyrope to 100 kbar. Contributions to

984   Mineralogy and Petrology, 129, 35-42.

985   Maldener, J., Hösch, A., Langer, K., and Rauch, F. (2003) Hydrogen in some natural garnets

986   studied by nuclear reaction analysis and vibrational spectroscopy. Physics and Chemistry

987   of Minerals, 30, 337-344.

988   Manning, C.E., and Bird, D.K. (1990) Fluorian garnets from the host rocks of the Skaergaard

989   intrusion: implications for metamorphic fluid composition. American Mineralogist, 75,

990   859-873.

991   Mosenfelder, J.L., and Rossman, G.R. (2012) Fluorine in the mantle: the role of nominally

992   anhydrous minerals. American Geophysical Union, Fall Meeting 2012, Abstract FDI54A-

993   06.

994   Mosenfelder, J.L., and Rossman, G.R. (2013a) Analysis of hydrogen and fluorine in pyroxenes: I.

995   Orthopyroxene. American Mineralogist, 98, 1026-1041.

996   Mosenfelder, J.L., and Rossman, G.R. (2013b) Analysis of hydrogen and fluorine in pyroxenes:

997   part II. Clinopyroxene. American Mineralogist, 98, 1042-1054.

998   Mosenfelder, J.L., Le Voyer, M., Rossman, G.R., Guan, Y., Bell, D.R., Asimow, P.D., and Eiler,

999   J.M. (2011) Analysis of hydrogen in olivine by SIMS: evaluation of standards and

1000   protocol. American Mineralogist, 96, 1725-1741.

1001   Mosenfelder, J.L., Rossman, G.R., and Johnson, E.A. (2015) Hydrous species in feldspars: a

1002   reassessment based on FTIR and SIMS. American Mineralogist, 100, 1209-1221.

1003   Mosenfelder, J.L., Andrys, J.L., von der Handt, A., Kohlstedt, D.L., and Hirschmann, M.M.

1004   (2020) Hydrogen incorporation in plagioclase. Geochimica et Cosmochimica Acta, 277,

1005   87–110.

1006   O'Leary, J.A., Rossman, G.R., and Eiler, J.M. (2007) Hydrogen analysis in minerals by

1007   continous-flow mass spectrometry. American Mineralogist, 92, 1990-1997.

1008   Paterson, M.S. (1982) The determination of hydroxyl by infrared absorption in quartz, silicate

1009   glasses, and similar materials. Bulletin de Minéralogie, 105, 20-29.

1010   Phichaikamjornwut, B., Skogby, H., Ounchanum, P., Limtrakun, P., and Boonsoong, A. (2012)

1011   Hydrous components of grossular-andradite garnets from Thailand: thermal stability and

1012   exchange kinetics. European Journal of Mineralogy, 24, 107-121.

1013   Philippot, P., Chevallier, P., Chopin, C., and Dubessy, J. (1995) Fluid composition and evolution

1014   in coesite-bearing rocks (Dora-Maira massif, Western Alps): implications for element

1015   recycling during subduction. Contributions to Mineralogy and Petrology, 121, 29-44.

1016   Raepsaet, C., Bureau, H., Khodja, H., Aubaud, C., and Carraro, A. (2008) μ-ERDA

1017   developments in order to improve the water content determination in hydrous and

1018   nominally anhydrous mantle phases. Nuclear Instruments and Methods in Physics

1019   Research Section B: Beam Interactions with Materials and Atoms 266, 1333–1337.

1020   Reynes, J., Jollands, M., Hermann, J., and Ireland, T. (2018) Experimental constraints on

1021   hydrogen diffusion in garnet. Contributions to Mineralogy and Petrology, 173, 69.

1022　Reynes, J., Lanari, P., and Hermann, J. (2020) A mapping approach for the investigation of Ti–

1023　　　OH relationships in metamorphic garnet. Contributions to Mineralogy and Petrology, 175,

1024　　　46.

1025　Roberge, M., Bureau, H., Bolfan-Casanova, N., Frost, D.J., Raepsaet, C., Surble, S., Khodja, H.,

1026　　　Auzende, A.-L., Fiquet, G. (2015) Is the transition zone a deep reservoir for fluorine?

1027　　　Earth and Planetary Science Letters, 429, 25-32.

1028　Rossman, G.R. (2006) Analytical methods for measuring water in nominally anhydrous minerals.

1029　　　In H. Keppler and J. R. Smyth, Eds., Water in Nominally Anhydrous Minerals, 62, p. 1-

1030　　　28. Reviews in Mineralogy and Geochemistry, Mineralogical Society of America,

1031　　　Chantilly, Virginia.

1032　Rossman, G.R., and Aines, R.D. (1986) Spectroscopy of birefringent grossular from Asbestos,

1033　　　Quebec, Canada. American Mineralogist, 71, 779-780.

1034　Rossman, G.R., and Aines, R.D. (1991) The hydrous components in garnets: grossular-

1035　　　hydrogrossular. American Mineralogist, 76, 1153-1164.

1036　Rossman, G.R., Beran, A., and Langer, K. (1989) The hydrous component of pyrope from the

1037　　　Dora Maira Massif, Western Alps. European Journal of Mineralogy, 1, 151–154.

1038　Schingaro, E., Lacalamita, M., Mesto, E., Ventruti, G., Pedrazzi, G., Ottolini, L., and Scordari., F.

1039　　　(2016) Crystal chemistry and light elements analysis of Ti-rich garnets. American

1040　　　Mineralogist, 101, 371-384.

1041　Slack, G.A., and Chrenko, R.M. (1971) Optical absorption of natural garnets from 1000 to 30000

1042　　　wavenumbers. Journal of the Optical Society of America, 61, 1325-1329.

1043   Smyth, J.R., Madel, R.E., McCormick, T.C., Munoz, J.L., and Rossman, G.R. (1990) Crystal-

1044   structure refinement of a F-bearing spessartine garnet. American Mineralogist, 75, 314-

1045   318.

1046   Sykes, D., Rossman, G., Veblen, D., and Grew, E. (1994) Enhanced H and F incorporation in

1047   borian olivine. American Mineralogist, 79, 904–908.

1048   Tenner, T.J., Hirschmann, M.M., Withers, A.C., and Hervig, R.L. (2009) Hydrogen partitioning

1049   between nominally anhydrous upper mantle minerals and melt between 3 and 5 GPa.

1050   Chemical Geology, 262, 42–56.

1051   Umemoto K., Wentzcovitch R.M., Hirschmann M.M., Kohlstedt D.L., and Withers A.C. (2011)

1052   A first-principles investigation of hydrous defects and IR frequencies in forsterite: the

1053   case for Si vacancies. American Mineralogist. 96, 1475-1479.

1054   Valley, J.W., Essene, E.J., and Peacor, D.R. (1983) Fluorine-bearing garnets in Adirondack calc-

1055   silicates. American Mineralogist, 68, 444-448.

1056   Verma, R.K. (1960) Elasticity of some high-density crystals. Journal of Geophysical Research 65,

1057   757-766.

1058   Vermeesch, P. (2018) IsoplotR: A free and open toolbox for geochronology. Geoscience

1059   Frontiers, 9, 1479-1493.

1060   Visser, D. (1993) Fluorine-bearing hydrogarnets from Blengsvatn, Bamble sector, South Norway.

1061   Mineralogy and Petrology, 47, 209-218.

1062   White, W.B., and Moore, R.K. (1972) Interpretation of the spin allowed bands of Fe^{2+} in silicate

1063   garnets. American Mineralogist, 57, 1692-1710.

1064   Withers, A.C., and Behrens, H. (1999) Temperature-induced changes in the NIR spectra of

1065   hydrous albitic and rhyolitic glasses between 300 and 100 K. Physics and Chemistry of

1066   Minerals, 27, 119-132.

1067   Withers, A.C., Wood, B.J., and Carroll, M.R. (1998) The OH content of pyrope at high pressure.

1068   Chemical Geology, 147, 161-171.

1069   Withers, A.C., Bureau, H., Raepsaet, C., and Hirschmann, M.M. (2012) Calibration of infrared

1070   spectroscopy by elastic recoil detection analysis of H in synthetic olivine. Chemical

1071   Geology, 334, 92-98.

1072   Witter, J.B., and Kuehner, S.M. (2004) A simple empirical method for high-quality electron

1073   microprobe analysis of fluorine at trace levels in Fe-bearing minerals and glasses.

1074   American Mineralogist, 89, 57-63.

1075   York, D., Evensen, N.M., Martínez, M.L., and De Basebe Delgado, J. (2004) Unified equations

1076   for the slope, intercept, and standard errors of the best straight line. American Journal of

1077   Physics, 72, 367-375.

1078   Yoshino, T. and Vazhakuttiyakam, J. (2018) Fluorine solubility in bridgmanite: A potential

1079   fluorine reservoir in the Earth's mantle. Earth and Planetary Science Letters, 504, 106-

1080   114.

1081   Zeng, Q., and Stebbins, J.F. (2000) Flourine sites in aluminosilicate glasses: High resolution ^{19}F

1082   NMR results. American Mineralogist, 85, 863–867.

1083   Zhang, C., Koepke, J., Wang, L-X., Wolff, P.E., Wilke, S., Stechern, A., Almeev, R., and Holtz,

1084   F. (2016) A practical method for accurate measurement of trace level fluorine in Mg- and

1085   Fe-Bearing minerals and glasses using electron probe microanalysis. Geostandards and

1086   Analytical Research, doi: 10.1111/j.1751-908X.2015.00390.x.

1087

1088 **TABLES**

1089 **Table 1.** Garnet sample localities and FTIR data

1090 **Table 2.** Results of elastic recoil detection analysis compared to other H calibration techniques

1091 **Table 3.** SIMS data

1092 **Table 4.** EPMA data and calculated garnet end members

1093

1094 **FIGURE CAPTIONS**

1095

1096 **FIGURE 1.** Representative FTIR spectra for grossular spectral classes 2, 2b, 3, 4, and 7. Class

1097 designations follow Rossman and Aines (1991). Spectra are plotted without baseline correction

1098 and offset from each other for clarity. Spectra in **a** and **b** are normalized to 1 cm; spectra in **c** are

1099 normalized to different thicknesses (as labeled) to facilitate comparison. (**a**) Class 2 (GRR42),

1100 with the strongest peak at 3647 cm^{-1}, and class 2b (GRR1386). Class 2b has peaks below 3620

1101 cm^{-1} that are almost absent in GRR42. Room temperature spectrum of GRR1386 (solid black

1102 curve) is directly overlain by spectrum taken at 77 K (grey dashed curve). (**b**) Class 2b

1103 (GRR732) and class 7 (GRR1122). Although these spectra have bands at similar positions, in

1104 class 7 the dominant peaks are at lower frequencies and the strongest peak is at 3599 cm^{-1} rather

1105 than 3647 cm^{-1}. (**c**) Class 3 and 4 spectra of natural and synthetic grossular garnets. Three

1106 representative spectra of JLM83a are displayed, with integrated absorbances (Abs_{tot}) equal to 691

1107 (dotted line), 1118 (dashed line), and 1526 cm^{-2} (solid line). The spectrum of GRR53 is from the

1108 slice labeled "GRR53B-F" displayed in Figure 6 of Rossman and Aines (1991). Spectra of

1109 synthetic, end-member grossular crystals are from Geiger and Armbruster (1997) and Withers et

1110 al. (1998). Spectral classes 3 and 4 are nominally distinguished by whether the strongest peak is

1111 at 3631 or 3621 cm^{-1}, respectively. Three of these garnets (GRR53, JLM83a, and the grossular

1112   made by Geiger and Armbruster) have strong peaks at 3689, 3677, 3665, and/or 3559 cm^{-1} that

1113   are weak or absent in the other two samples (GRR1537 and the grossular synthesized by Withers

1114   et al.).

1115

1116

1117   **FIGURE 2.** Detailed comparison near the baselines of 77 K and 298 K spectra of GRR1386.

1118   The band at ~3240 cm^{-1} at 77 K is attributed to frozen H_2O in fluid inclusions. Bands attributed

1119   to structural OH$^-$ groups are off scale. Spectra of liquid water from Bertie and Lan (1996) and ice

1120   from Johnson and Rossman (2003) also plotted for comparison. GRR1386 spectra are

1121   normalized to 1 cm thickness; spectra of ice and water are arbitrarily scaled.

1122

1123   **FIGURE 3.** Raw (uncorrected) H_2O concentrations determined by ERDA for three East African

1124   grossular garnets (GRR732, GRR771, and GRR1756) and blank forsterite (GRR1017), as a

1125   function of integrated absorbance (Abs_{tot}). Solid line is a York regression. Dashed lines represent

1126   95% confidence intervals calculated from *a priori* errors. Equation and mean squared weighted

1127   deviation (MSWD) of the fit are also shown.

1128

1129   **FIGURE 4.** $^{16}OH/^{18}O$ data from two SIMS sessions. Error bars not shown are within the symbol

1130   size. Solid lines are York regressions fit to data (circles) on the blank and East African samples

1131   only, with 95% confidence intervals (calculated from *a priori* errors) displayed as dashed curves.

1132   The equation and MSWD for each regression are also displayed in the graphs. **(a)** 2012 data.

1133   Each point represents the average of three to five measurements, with $2s_x$ (sample standard

1134   deviation) error bars displayed for $^{16}OH/^{18}O$. **(b)** 2016 data. In this plot, each point represents a

1135 single analysis. Consequently, uncertainties in $^{16}OH/^{18}O$ ($2s_{\bar{x}}$, standard error of the mean) are all

1136 within the symbol size in this plot. Some data points are obscured by overlap with other data; all

1137 original data are given in the supplementary material.

1138

1139 **FIGURE 5.** Backscattered electron image of JLM83a after SIMS analysis. H_2O and F

1140 concentrations (in µg/g) are displayed above (up and to the left) each SIMS crater (black spot).

1141 Analysis numbers in order of collection are labeled to the lower right of each spot.

1142 The analyses with asterisks (analyses 15-18) were compromised by elevated background $^{16}OH^-$

1143 and $^{19}F^-$, as discussed in the text. Cycle profiles (uncalibrated depth profiles) for analyses 12 and

1144 20 are displayed in supplementary Figure S8.

1145

1146 **FIGURE 6.** Correlations between ^{16}OH and ^{19}F for grossular and spessartine. (**a**) SIMS data for

1147 grossular from sessions in 2012 (open symbols) and 2016 (closed symbols). Each symbol

1148 represents a single analysis ($2s_{\bar{x}}$ uncertainties are within the symbol size for each point). Solid

1149 lines are ordinary least-squares (OLS) regressions to data for East African grossular garnets ($r^2 =$

1150 0.98) and multiple analyses on Asbestos grossular JLM83a ($r^2 = 0.99$). Data on JLM83a that were

1151 compromised by contamination (Fig. 5) are not included in this plot. (**b**) Spessartine data from

1152 2012 session. Each data point on this plot represents an average of between four and 11 analyses

1153 for one sample ($2s_x$ uncertainties are within the symbol size). Solid line is an OLS regression (r^2

1154 = 0.99) to all of the data.

1155

1156

1157 **FIGURE 7.** Comparison of ERDA results (circles) to previous calibration data on Asbestos

1158 grossular (GRR53 and GRR53B, triangles; Aines and Rossman 1984; Rossman and Aines 1991),

1159 Maldener et al. (2003, diamonds), and O'Leary et al. (2007, square). Only two data points from

1160 the compilation of Rossman and Aines (1991) are plotted (for Asbestos garnets GRR53 and

1161 GRR53F), but the original regression determined for their entire data set of grossular and

1162 hydrogrossular garnets over a much wider range of H contents (up to 12.75 wt% H_2O) is

1163 displayed as a dashed line. The ERDA data have been blank corrected in this graph by

1164 subtracting 100 μg/g from the raw values plotted in Figure 3.

1165

1166 **FIGURE 8.** Results of spectral curve fitting plotted as function of calculated F (per formula unit).

1167 Frequencies of fitted bands vary by up to 3 cm^{-1}. Symbols (see inset legend in **a**) correspond to

1168 those in Figure 7. **(a)** Integrated absorbance *vs.* F for fitted bands centered at ~3631, 3643, 3647,

1169 3657, 3664, 3674, and 3688 cm^{-1}. **(b)** Integrated absorbance vs. F for fitted bands centered at

1170 ~3530, 3539, 3545, 3560, 3567, 3582, 3600, 3608, and 3622 cm^{-1}.

1171

1172

1173

1174

1175

1176

1177

1178

1179

1180 **FIGURES**
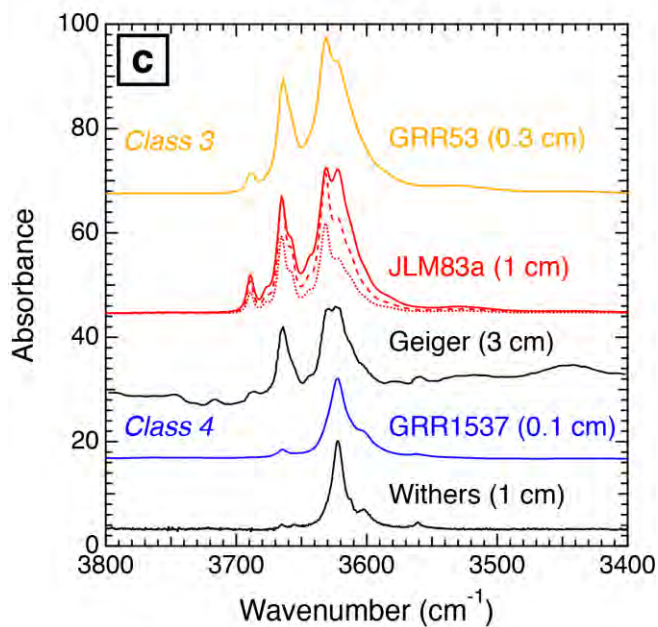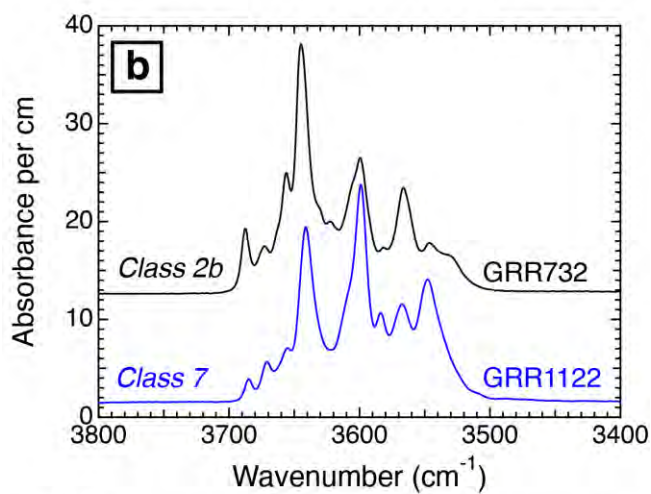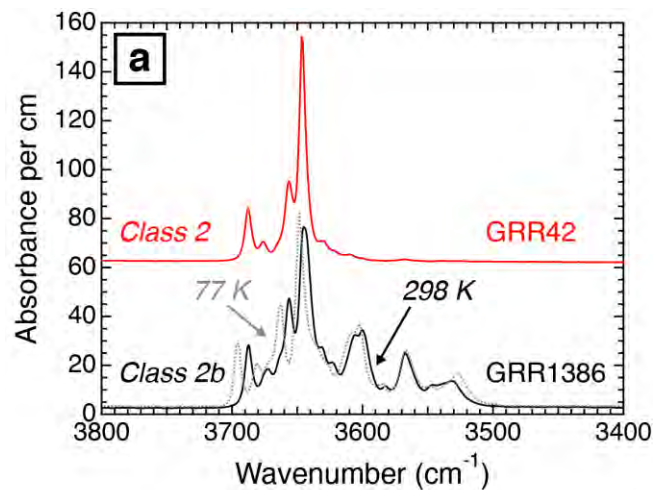
1181

1182   **FIGURE 1.** Representative FTIR spectra for grossular spectral classes 2, 2b, 3, 4, and 7. Class

1183   designations follow Rossman and Aines (1991). Spectra are plotted without baseline correction

1184   and offset from each other for clarity. Spectra in **a** and **b** are normalized to 1 cm; spectra in **c** are

1185   normalized to different thicknesses (as labeled) to facilitate comparison. (**a**) Class 2 (GRR42),

1186   with the strongest peak at 3647 cm^{-1}, and class 2b (GRR1386). Class 2b has peaks below 3620

1187 cm^{-1} that are almost absent in GRR42. Room temperature spectrum of GRR1386 (solid black

1188   curve) is directly overlain by spectrum taken at 77 K (grey dashed curve). (**b**) Class 2b

1189   (GRR732) and class 7 (GRR1122). Although these spectra have bands at similar positions, in

1190   class 7 the dominant peaks are at lower frequencies and the strongest peak is at 3599 cm^{-1} rather

1191   than 3647 cm^{-1}. (**c**) Class 3 and 4 spectra of natural and synthetic grossular garnets. Three

1192   representative spectra of JLM83a are displayed, with integrated absorbances (Abs_{tot}) equal to 691

1193   (dotted line), 1118 (dashed line), and 1526 cm^{-2} (solid line). The spectrum of GRR53 is from the

1194   slice labeled "GRR53B-F" displayed in Figure 6 of Rossman and Aines (1991). Spectra of

1195   synthetic, end-member grossular crystals are from Geiger and Armbruster (1997) and Withers et

1196   al. (1998). Spectral classes 3 and 4 are nominally distinguished by whether the strongest peak is

1197   at 3631 or 3621 cm^{-1}, respectively. Three of these garnets (GRR53, JLM83a, and the grossular

1198   made by Geiger and Armbruster) have strong peaks at 3689, 3677, 3665, and/or 3559 cm^{-1} that

1199   are weak or absent in the other two samples (GRR1537 and the grossular synthesized by Withers

1200   et al.).

1201

1202

1203

1204

1205

1206
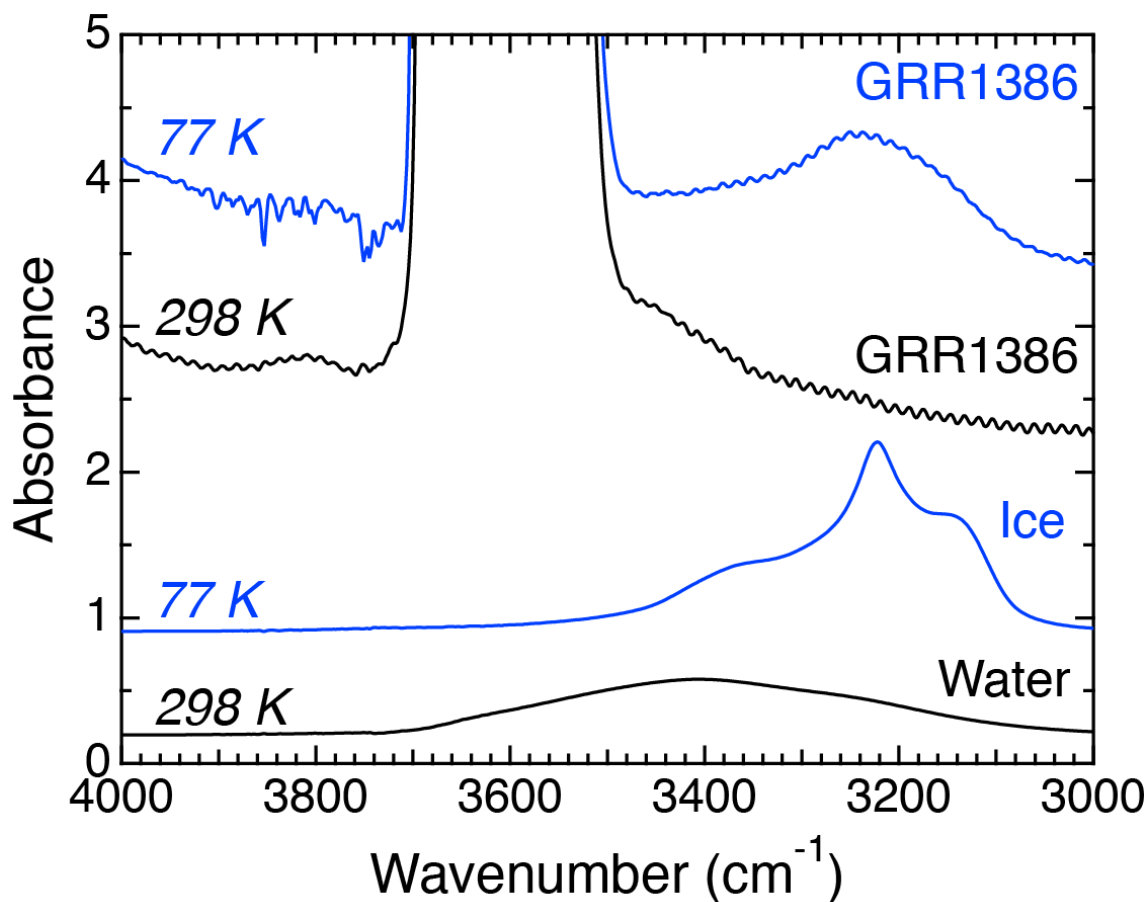
1207

1208 **FIGURE 2.** Detailed comparison near the baselines of 77 K and 298 K spectra of GRR1386.

1209 The band at ~3240 cm^{-1} at 77 K is attributed to frozen H_2O in fluid inclusions. Bands attributed

1210 to structural OH$^-$ groups are off scale. Spectra of liquid water from Bertie and Lan (1996) and ice

1211 from Johnson and Rossman (2003) also plotted for comparison. GRR1386 spectra are

1212 normalized to 1 cm thickness; spectra of ice and water are arbitrarily scaled.

1213
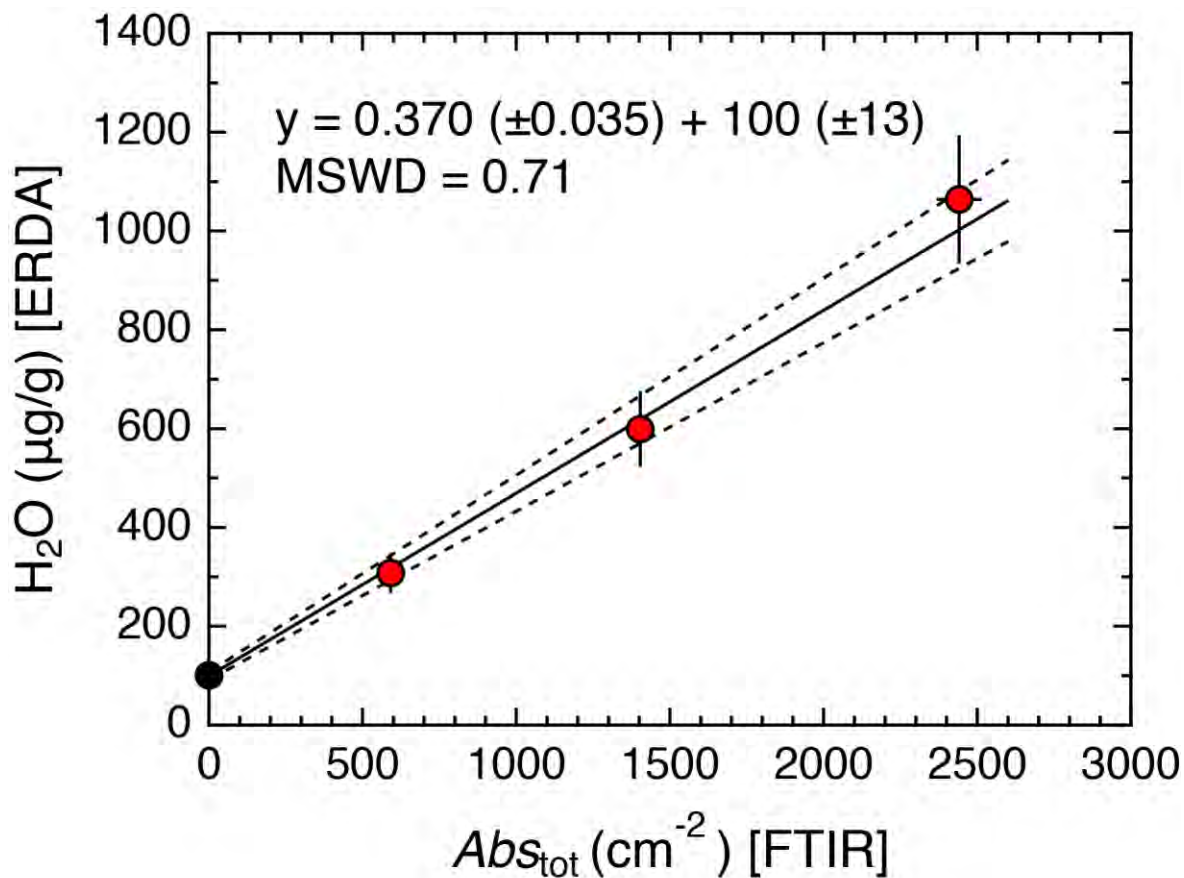
FIGURE 3. Raw (uncorrected) H_2O concentrations determined by ERDA for three East African grossular garnets (GRR732, GRR771, and GRR1756) and blank forsterite (GRR1017), as a function of integrated absorbance (Abs_{tot}). Solid line is a York regression. Dashed lines represent 95% confidence intervals calculated from *a priori* errors. Equation and mean squared weighted deviation (MSWD) of the fit are also shown.
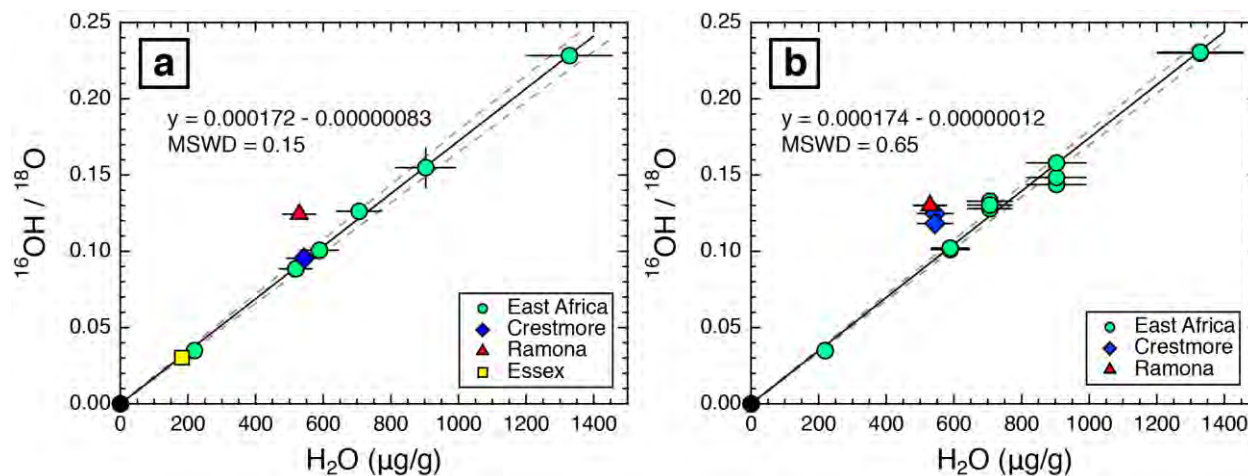
1224

1225 **FIGURE 4.** $^{16}OH/^{18}O$ data from two SIMS sessions. Error bars not shown are within the symbol

1226 size. Solid lines are York regressions fit to data (circles) on the blank and East African samples

1227 only, with 95% confidence intervals (calculated from *a priori* errors) displayed as dashed curves.

1228 The equation and MSWD for each regression are also displayed in the graphs. **(a)** 2012 data.

1229 Each point represents the average of three to five measurements, with $2s_x$ (sample standard

1230 deviation) error bars displayed for $^{16}OH/^{18}O$. **(b)** 2016 data. In this plot, each point represents a

1231 single analysis. Consequently, uncertainties in $^{16}OH/^{18}O$ ($2s_{\bar{x}}$, standard error of the mean) are all

1232 within the symbol size in this plot. Some data points are obscured by overlap with other data; all

1233 original data are given in the supplementary material.

1234

1235

1236

1237

1238

1239

1240
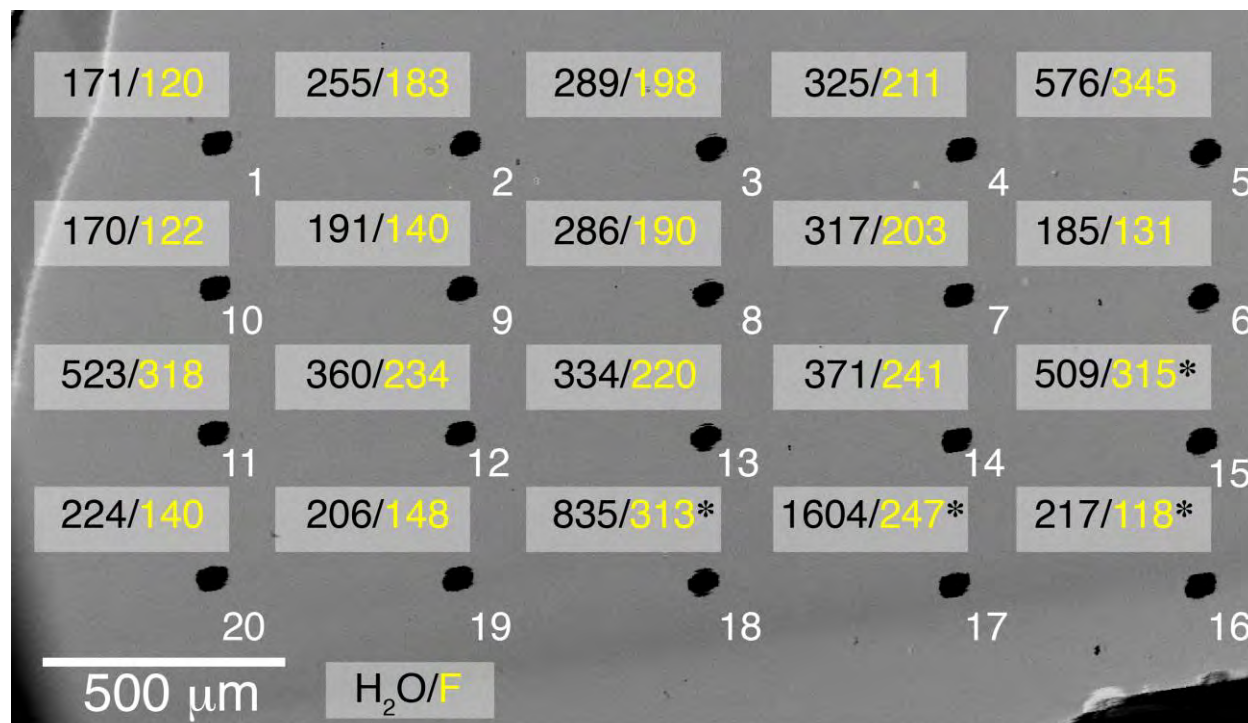
1241

1242 **FIGURE 5.** Backscattered electron image of JLM83a after SIMS analysis. H_2O and F

1243 concentrations (in μg/g) are displayed above (up and to the left) each SIMS crater (black spot).

1244 Analysis numbers in order of collection are labeled to the lower right of each spot.

1245 The analyses with asterisks (analyses 15-18) were compromised by elevated background $^{16}OH^-$

1246 and $^{19}F^-$, as discussed in the text. Cycle profiles (uncalibrated depth profiles) for analyses 12 and

1247 20 are displayed in supplementary Figure S8.

1248

FIGURE 6. Correlations between ^{16}OH and ^{19}F for grossular and spessartine. (**a**) SIMS data for grossular from sessions in 2012 (open symbols) and 2016 (closed symbols). Each symbol represents a single analysis ($2s_{\bar{x}}$ uncertainties are within the symbol size for each point). Solid lines are ordinary least-squares (OLS) regressions to data for East African grossular garnets ($r^2 = 0.98$) and multiple analyses on Asbestos grossular JLM83a ($r^2 = 0.99$). Data on JLM83a that were compromised by contamination (Fig. 5) are not included in this plot. (**b**) Spessartine data from 2012 session. Each data point on this plot represents an average of between four and 11 analyses for one sample ($2s_x$ uncertainties are within the symbol size). Solid line is an OLS regression ($r^2 = 0.99$) to all of the data.

1265

1266   **FIGURE 7.** Comparison of ERDA results (circles) to previous calibration data on Asbestos

1267   grossular (GRR53 and GRR53B, triangles; Aines and Rossman 1984; Rossman and Aines 1991),

1268   Maldener et al. (2003, diamonds), and O'Leary et al. (2007, square). Only two data points from

1269   the compilation of Rossman and Aines (1991) are plotted (for Asbestos garnets GRR53 and

1270   GRR53F), but the original regression determined for their entire data set of grossular and

1271   hydrogrossular garnets over a much wider range of H contents (up to 12.75 wt% H_2O) is

1272   displayed as a dashed line. The ERDA data have been blank corrected in this graph by

1273   subtracting 100 µg/g from the raw values plotted in Figure 3.

1274

1275

1276

1277

1278
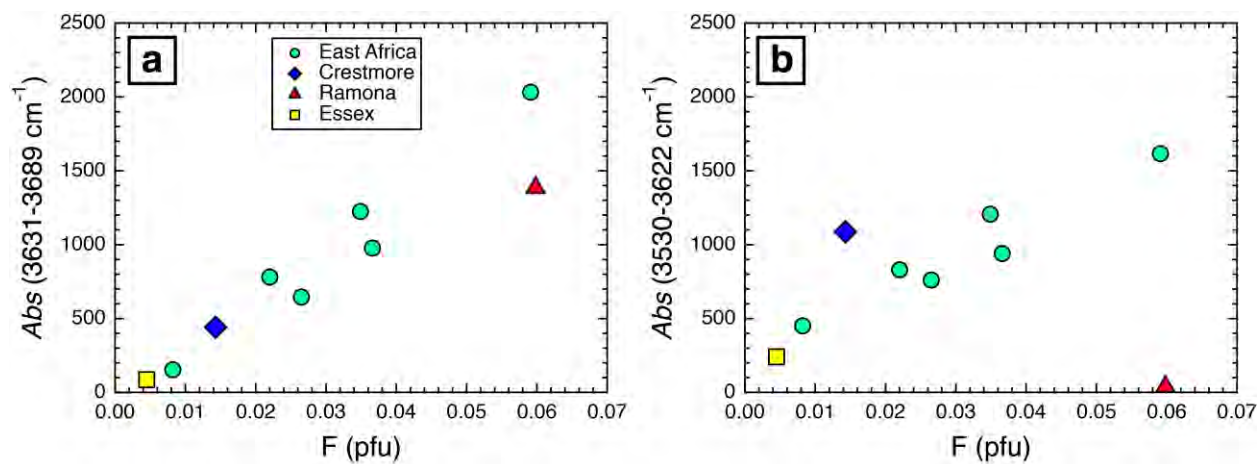
1279

1280 **FIGURE 8.** Results of spectral curve fitting plotted as function of calculated F (per formula unit).

1281 Frequencies of fitted bands vary by up to 3 cm^{-1}. Symbols (see inset legend in **a**) correspond to

1282 those in Figure 7. **(a)** Integrated absorbance *vs.* F for fitted bands centered at ~3631, 3643, 3647,

1283 3657, 3664, 3674, and 3688 cm^{-1}. **(b)** Integrated absorbance vs. F for fitted bands centered at

1284 ~3530, 3539, 3545, 3560, 3567, 3582, 3600, 3608, and 3622 cm^{-1}.

1285

1286

1287

1288

1289

Table 1: Garnet sample localities and FTIR data				
Sample No.	Locality	Spectral class[a]	Abs_{tot} (cm^{-2})	Mean wavenumber (cm^{-1})
GRR42	Ramona Mine, California, U.S.A.	2	1430(14)	3647
GRR229	Stream gravel, Merelani Hills, Tanzania	2b	1909(38)	3623
GRR732	Mindi Hills, Kenya	2b	1403(28)	3617
GRR771	Merelani Hills, Tanzania	2b	2441(73)	3622
GRR1122	Crestmore Mine, California, U.S.A.	7	1471(44)	3597
GRR1386	Stream gravel, Merelani Hills, Tanzania	2b	3589(72)	3633
GRR1386a	Stream gravel, Merelani Hills, Tanzania	2b	1592(48)	3619
GRR1429	Essex Country, New York, U.S.A.	7	493(38)	3570-3579[b]
GRR1756	#2 reef, Scorpion Mine, Voi, Taita, Kenya	7	591(12)	3595
JLM83a	Asbestos, Quebec, Canada	3	691-1544[c]	3630-3631[c]
Notes: uncertainties in parentheses are estimated as discussed in text.				
[a] Classification scheme of Rossman and Aines (1991)				
[b] Range of values for 7 spectra				
[c] Range measured in 48 spectra				

Table 2: Results of elastic recoil detection analysis (ERDA) compared to other H calibration techniques

Sample No.	Phase	Abs_{tot} (cm^{-2})	H$_2$O, µg/g		Reference	Method
			Uncorrected	Blank corrected		
GRR1756	Grossular	591(12)	308(40)	208(40)	This study	ERDA
GRR732	Grossular	1403(28)	599(76)	499(76)	This study	ERDA
			–	1062(31)	1	CFMS
GRR771	Grossular	2441(73)	1064(130)	964(130)	This study	ERDA
NSL1	Rhyolitic glass		11,133(1399)	11,033 (1399)	This study	ERDA
			–	11,600	2	KFT-FTIR
N3	Rhyolitic glass		33,658 (4209)	33,558 (4209)	This study	ERDA
			–	33,000	2	KFT-FTIR
N5	Rhyolitic glass		50,549 (6313)	50,449 (6313)	This study	ERDA
			–	50,600	2	KFT-FTIR
GRR1017 [a]	Forsterite	0	101(14)	0	This study	ERDA
GRR53	Grossular	2877	–	1800	3, 4	MEA, MAN
GRR53F	Grossular	4796	–	2800	4	^{19}F NRA
HESS1	Grossular	2510	–	870	5	^{15}N NRA
		2006	–	950	5	^{15}N NRA
TSAV	Grossular	1208	–	480	5	^{15}N NRA
MALI	Grossular	168	–	170	5	^{15}N NRA
GRMALI	Grossular	77	–	190	5	^{15}N NRA

Notes: References: 1 = O'Leary et al. (2007); 2= Tenner et al. (2009); 3 = Aines and Rossman (1984); 4 = Rossman and A
CFMS = continuous-flow mass spectrometry; KFT-FTIR = Karl-Fischer titration and FTIR; MEA = P$_2$O$_5$ coulometry (mo
Uncertainties in parentheses are 2s in terms of least units cited

[a]Blank reference material used to correct ERDA data.

ines (1991); 5 = Maldener et al. (2003)

isture evolution analyzer); MAN = evolved H_2 gas volume (manometry); NRA = nuclear reaction analysis

Table 3: SIMS data

Sample no.	SIMS session	No. of analyses	H_2O, µg/g [a]	$^{16}O^1H/^{18}O$
GRR1122-HT	2012	4	0	0.000338 – 0.000450 [c]
	2016	3	0	0.001365 – 0.001904 [c]
GRR42	2012	5	529(50)	0.1244(14)
	2016	2[d]		0.1300, 0.1302
GRR229	2012	4	706(68)	0.1262(16)
	2016	3		0.1304(49)
GRR732	2012	4	519(50)	0.0885(16)
GRR771	2012	4	903(90)	0.155(13)
	2016	3		0.150(15)
GRR1122	2012	4	544(54)	0.0956(12)
	2016	2[d]		0.1183, 0.1247
GRR1386	2012	4	1328(128)	0.2283(31)
	2016	3		0.2302(6)
GRR1386a	2012	4	589(58)	0.1007(23)
	2016	3		0.1016(10)
GRR1429	2012	4	182(22)	0.0303(34)
GRR1756	2012	4	219(21)	0.0349(2)
	2016	2[d]		0.349, 0.349[d]
JLM83a[e]	2016	16[f]	256-571	0.0296–0.1002

Notes: Numbers in parentheses are $2s$ uncertainties in terms of least units cited.

[a] Values calculated from FTIR using calibration factor of 0.37 (Eq. 1), with uncertainties propag

[b] Values calculated from $^{16}O^1H/^{18}O$ using working curve for F-bearing glasses.

[c] Uncorrected ratios, given as a range.

[d] For samples with only two analyses, each analysis is given (separated by comma).

[e] Values for this sample are given as a range (for both FTIR and SIMS analyses).

[f] Four analyses were rejected owing to a spike in the blank, as described in the text.

$^{19}F/^{18}O$	F, µg/g [b]
1.279(21)	508 (8)
1.325(40)	537(84)
6.563(69)	2606(27)
6.529, 6.584	2559, 2581
3.713(48)	1474(19)
3.751(57)	1470(22)
2.819(49)	1119(19)
4.14(19)	1644(75)
3.99(10)	1565(39)
1.281(16)	508(6)
1.295, 1.447	508, 567
6.824(49)	2709(19)
6.694(64)	2624(25)
2.422(48)	962(19)
2.423(16)	950(6)
0.465(34)	185(13)
0.602(4)	239(2)
0.611, 0.615[d]	239, 241
0.3502–0.8789	120–345

ɟated as described in text.

Table 4: EPMA data and calculated garnet end members

Sample No.	GRR42	GRR229	GRR732	GRR771	GRR1122
SiO_2	38.59(24)	38.77(24)	40.15(39)	39.84(18)	38.69(31)
TiO_2	–	0.40(3)	0.34(3)	0.54(2)	0.57(6)
Al_2O_3	21.43(12)	20.94(13)	21.97(28)	22.34(8)	17.64(7)
Cr_2O_3	–	0.28(2)	0.04(3)	–	–
V_2O_3	–	1.90(3)	0.88(1)	0.05(2)	–
FeO^a	3.23(2)	0.08(1)	0.06(3)	0.14(2)	7.53(26)
MnO	0.10(2)	0.90(5)	1.15(1)	0.27(3)	0.38(4)
MgO	–	0.47(2)	0.54(3)	0.34(1)	0.07(2)
CaO	35.33(6)	35.10(14)	35.44(33)	36.25(10)	34.61(20)
H_2O^+	0.0723^b	0.0706^c	0.0519^c	0.0903^c	0.0544^c
F	0.2477(36)	0.1516(30)	0.1119^e	0.1470(62)	0.0586(62)
O=F	-0.1	-0.06	-0.05	-0.06	-0.02
Total	98.90	99.00	100.68	99.95	99.58
Recalculated					
FeO	1.16	0.08	0.06	0.14	2.09
Fe_2O_3	2.30	–	–	–	6.05
Recalculated Total^f	99.13	99.00	100.68	99.95	100.19
Si	2.9457	2.9576	3.0015	2.9906	2.9804
Ti	–	0.0230	0.0191	0.0305	0.0330
Al^{VI}	1.8978	1.8583	1.9357	1.9764	1.5924
Al^{IV}	0.0301	0.0243	–	–	0.0091
Cr	–	0.0169	0.0024	–	–
V	–	0.1162	0.0527	0.0030	–
Fe^{2+}	0.0738	0.0051	0.0038	0.0088	0.1346
Fe^{3+}	0.1324	–	–	–	0.3506
Mn	0.0065	0.0582	0.0728	0.0172	0.0248
Mg	–	0.0534	0.0602	0.0380	0.0080
Ca	2.8896	2.8689	2.8387	2.9155	2.8566
H_4	0.0092	0.0090	0.0065	0.0113	0.0070
O	11.9402	11.9699	12.0027	11.9959	11.9857
F	0.0598	0.0366	0.0265	0.0349	0.0143
End Members					
Katoite	0.31%	0.30%	0.22%	0.38%	0.23%
FCa garnet	0.50%	0.30%	0.22%	0.29%	0.12%

Schorlomite-Al	–	1.15%	–	–	0.45%
Morimotoite	–	–	–	–	2.40%
Majorite	–	–	–	–	–
Goldmanite	–	5.81%	2.64%	0.15%	–
Uvarovite	–	0.84%	0.12%	–	–
Spessartine	0.22%	1.94%	2.43%	0.57%	0.83%
Pyrope	–	1.78%	2.01%	1.27%	0.27%
Almandine	2.46%	0.17%	0.13%	0.29%	3.69%
Grossular	91.41%	87.22%	91.43%	96.02%	74.49%
Andradite	4.11%	–	–	–	17.53%
Remainder	1.00%	0.48%	0.82%	1.03%	0.00%
Total	100.01%	99.99%	100.02%	100.00%	100.01%

Notes: Cation assignments and garnet end members calculated using Locock (2008), on an 8

See Locock (2008) for definition of end members. "Remainder" represents the proportion of ca

Dashed lines denote oxides, elements or end members below detection limit or calculated to b

EPMA data represent averages (in wt%, with 1s uncertainties in parentheses) of 5 to 6 analys

[a] Total Fe calculated as FeO.

[b] H_2O calculated from 2012 SIMS data, using fit to data for East African grossulars.

[c] H_2O calculated from FTIR data (Table 3).

[d] H_2O and F based on 2016 SIMS data, for two analyses at extreme ends of range.

[e] F based on 2012 SIMS data.

[f] Recalculated wt% total after calculation of Fe^{2+}/Fe^{3+}.

GRR1386	GRR1386a	GRR1429	GRR1756	JLM83a	
				low	*high*
39.19(23)	39.96(5)	39.48(16)	39.70(11)	39.95(18)	39.95(18)
0.64(3)	0.36(3)	0.42(3)	0.40(1)	–	–
22.29(7)	21.90(5)	18.62(13)	20.90(12)	22.23(13)	22.23(13)
–	–	–	0.29(2)	–	–
–	–	–	1.77(5)	–	–
0.20(3)	1.36(5)	7.27(9)	0.06(1)	1.82(10)	1.82(10)
0.14(2)	0.33(2)	0.21(2)	0.97(1)	0.24(3)	0.24(3)
0.43(1)	0.31(1)	0.14(1)	0.57(1)	–	–
36.27(11)	35.78(6)	34.11(9)	35.02(5)	35.51(14)	35.51(14)
0.1328[c]	0.0589[c]	0.0182[c]	0.0219[c]	0.0171[d]	0.0576[d]
0.2478(24)	0.0924(29)	0.0185[e]	0.0343(42)	0.012[d]	0.0345[d]
-0.10	-0.04	-0.01	-0.01	-0.01	-0.01
99.44	100.11	100.28	99.73	99.77	99.83
0.2	1.36	3.48	0.06	1.82	1.82
–	–	4.22	–	–	–
99.44	100.11	100.71	99.73	99.77	99.83
2.9536	3.0037	3.0137	3.0079	3.0162	3.0138
0.0363	0.0204	0.0241	0.0228	–	–
1.9650	1.9401	1.6752	1.8663	1.9781	1.9765
0.0149	–	–	–	–	–
–	–	–	0.0174	–	–
–	–	–	0.1075	–	–
0.0126	0.0855	0.2219	0.0038	0.1149	0.1148
–	–	0.2422	–	–	–
0.0089	0.0210	0.0136	0.0622	0.0153	0.0153
0.0483	0.0310	0.0022	0.0644	–	–
2.9289	2.8817	2.7899	2.8429	2.8726	2.8703
0.0167	0.0074	0.0023	0.0028	0.0022	0.0072
11.9523	11.9850	11.9955	12.0229	12.0053	12.0031
0.0591	0.0220	0.0045	0.0082	0.0029	0.0082
0.56%	0.25%	0.08%	0.09%	0.07%	0.24%
0.49%	0.18%	0.04%	0.07%	0.02%	0.07%

0.75%	–	–	–	–	–
–	2.04%	2.41%	–	–	–
–	0.37%	0.07%	–	–	–
–	–	–	5.38%	–	–
–	–	–	0.87%	–	–
0.30%	0.70%	0.45%	2.07%	0.51%	0.51%
1.61%	0.66%	–	2.15%	–	–
0.42%	1.78%	6.36%	0.13%	3.64%	3.50%
94.87%	93.43%	76.83%	88.36%	94.66%	94.50%
–	–	12.11%	–	–	–
1.00%	0.59%	1.65%	0.89%	1.10%	1.18%
100.00%	100.00%	100.00%	100.01%	100.00%	100.00%

cation basis (treating H as H_4^{4+}).

ations that could not be allocated.

be 0.

es for all samples except JLM83a (average of 36 analyses).